The Influence of Large-Scale Weather Patterns on Potential Wind Energy Fields over Mexico

Victor M. Peñaranda-Vélez
Institute for Atmospheric Sciences and Climate Change
Universidad Nacional Autónoma de México
Investigación Científica s/n, C.U., 04510
victor.penaranda@atmosfera.unam.mx

Carlos A. Ochoa-Moya
Institute for Atmospheric Sciences and Climate Change
Universidad Nacional Autónoma de México
Investigación Científica s/n, C.U., 04510
carlos.ochoa@atmosfera.unam.mx

Arturo I. Quintanar
Institute for Atmospheric Sciences and Climate Change
Universidad Nacional Autónoma de México
Investigación Científica s/n, C.U., 04510
arturo.quintanar@atmosfera.unam.mx

THE INFLUENCE OF LARGE-SCALE WEATHER PATTERNS ON POTENTIAL WIND ENERGY FIELDS OVER MEXICO

Victor M. Peñaranda-Vélez
Institute for Atmospheric Sciences and Climate Change
Universidad Nacional Autónoma de México
Investigación Científica s/n, C.U., 04510
victor.penaranda@atmosfera.unam.mx

Carlos A. Ochoa-Moya
Institute for Atmospheric Sciences and Climate Change
Universidad Nacional Autónoma de México
Investigación Científica s/n, C.U., 04510
carlos.ochoa@atmosfera.unam.mx

Arturo I. Quintanar
Institute for Atmospheric Sciences and Climate Change
Universidad Nacional Autónoma de México
Investigación Científica s/n, C.U., 04510
arturo.quintanar@atmosfera.unam.mx

September 25, 2026

ABSTRACT

The assessment of wind energy resources in large regions presents a substantial challenge for energy system operators due to the intricacies involved in accurately describing all atmospheric circulation patterns and, even more so, modeling their inherent dynamics. This research primarily aimed to identify the prevailing synoptic weather patterns over continental Mexico and its surrounding regions. The study utilized ERA5 Reanalysis daily mean sea level pressure anomaly data and two widely recognized clustering techniques, k-means and self-organizing maps, to achieve this objective. Research findings indicate that four weather patterns, estimated using k-means clustering, are sufficient to explain daily atmospheric variability over continental Mexico. However, the fifteen weather patterns identified through the self-organizing-maps technique suggest that the k-means-determined patterns can be complemented by interconnected transition patterns, which represent a more intricate dynamics within the tropical and subtropical atmosphere. The second primary objective of this research is to assess and analyze the impact of weather patterns on the wind velocity field and energy availability across continental Mexico. This assessment employed a probabilistic methodology grounded in the L-moments theory and the inference of a regional wind-speed model, which was supported by the Weibull and Kappa distributions. The findings indicate that fluctuations in large-scale weather patterns across the continental Mexican influence the potential wind energy production significantly. For instance, in the Oaxaca region, the potential wind energy fluctuates between 189 and 734 W/m^2. These results emphasize the crucial influence of these weather patterns on energy production and highlight the need for a comprehensive study within a forecasting framework to enhance the current operation of the Mexican electrical system.

***K*eywords** Wind Energy · Weather Patterns · Climatology · Regional Analysis · ERA5 · L-moments · Self-organizing Maps · K-means clustering · Kappa distribution for indexing

1 Introduction

Climate variability significantly impacts the energy production and various economic sectors of Mexico. As observed, energy consumption in the Mexican Electrical System (MES) has increased by approximately 3.4% over the past few years [1]. This trend necessitates implementing programs and policies to enhance and modernize the technologies used to extract and convert natural resources for energy production. To achieve balanced, reliable, efficient, and sustainable planning for energy programs, it is imperative to understand how short- and long-term weather variability affects the energy MES infrastructure. This knowledge is crucial for optimizing public funding investments and developing strategies to enhance the competitiveness of Mexican enterprises that necessitate the adoption of new sustainable energy technologies.

It is well known that climate factors, such as rainfall events and heat waves, are the most significant contributors to the modulation of electricity consumption across regions. Furthermore, in wind power systems, the variability of the wind speed field is primarily driven by weather-pattern dynamics [2]. Consequently, climate factors and weather patterns intricately influence the relationship between energy production and consumption. Mexico's wind energy production, accounting for 5.8% of total energy generation, is increasingly reliant on weather variability [3, 4]. In addition, the sparse spatial distribution of current Mexican wind farms poses challenges to maintaining the stability of the MES infrastructure and mitigating fluctuations in electricity prices.

The variability of weather patterns and their impact on the space-time dynamic of wind fields over Mexico have received limited study and assimilation. Although some studies have provided approximations of the classification of Mexico's weather patterns and their primary atmospheric forcing factors [5, 6, 7, 8, 9], the influence of these factors on wind energy production and their impact on the MES infrastructure remain to be fully understood. This has sparked our interest in conducting an assessment of different methods for identifying, classifying, and modeling large-scale weather patterns in the tropical and subtropical regions of Mexico, and assessing the impact of these weather patterns on available wind energy and the current MES infrastructure.

In this context, large-scale weather patterns (LSWP) are understood as synoptic atmospheric phenomena that characterize organized, evolving atmospheric processes, represented by modes or states [10], and occur and persist on timescales of about days. Certain persistent and recurrent LSWP are referred to as weather regimes in the scientific literature, and they are mainly characterized by their low-frequency variability in timescales ranging from days to weeks [11, 12]. It is evident that a comprehensive understanding of the temporal and spatial variability of low- and high-frequency LSWP is crucial for enhancing extended-range weather forecasting models and for forecasting Dunkelflaute or wind-power-ramp scenarios over wind energy systems [13, 14].

Despite extensive research on LSWP over the years [15, 16, 17, 18, 19, 20, 21, 6, 5, 22, 23, 13, 24, 25, 7, 11, 26, 10], the underlying process that explains the temporality and spatial occurrence of LSWP, irrespective of the LSWP detection technique, remains an open challenge. For instance, in mid-latitudes, the low-frequency variability of LSWP is characterized by transitional patterns between two primary persistent atmospheric states: blocking and zonal-flow regimes. Blocking regimes are LSWP characterized by anticyclonic quasi-stationary circulation systems that occur in either the Atlantic or the Pacific region, or both concurrently, and persist for days to weeks, obstructing westerly flows [27, 12, 28, 29, 10]. When these blocking LSWP occur, they can induce diverse weather phenomena, including heat waves, droughts, cold spells, and other extreme climate events [30, 31, 32]. This is primarily attributed to the radiative forcing under low-potential-vorticity anticyclonic circulation and the horizontal thermal advection near the center of a blocking anticyclone [33, 28]. In the energy sector, it is valuable to study the occurrence and duration of these blocking LSWP because they pose a significant risk of energy underproduction due to a substantial reduction in near-surface winds [13].

In Mexican territory, former researchers have proposed that at least ten distinct weather patterns characterize the dominant large-scale weather variability of Mexico, based on the analysis of surface pressure fluctuations [8]. Certain weather patterns are characterized by spatio-temporal variations in anticyclonic circulation systems over southern or southeastern Mexico. Other weather patterns arise from perturbations of easterly atmospheric waves, strong overland temperature gradients that induce meridional flow migrations, and atmospheric patterns resulting from the strengthening (or weakening) of westerly flows. Ochoa et al. [7], who used the Self-Organizing Maps clustering technique on mean sea-level pressure data to detect weather patterns, have suggested the existence of 20 prevailing weather patterns for Mexico and neighboring regions. Ochoa et al. [7] have elucidated that certain prevailing weather patterns in Mexico are intricately linked to the dynamics of the Atlantic anticyclonic circulation system, commonly referred to as the North Atlantic Subtropical High (NASH), and the Pacific anticyclonic system, also known as the North Pacific Subtropical High (NPSH). Furthermore, the weather patterns associated with NASH dynamics are closely linked to the Caribbean low-level jet and its intensification during the mid-summer dry spell.

Conversely, Thomas et al. [9] have identified eight dominant weather patterns for Mexico using the K-means clustering technique on 500-hPa geopotential height data. Thomas et al. [9] characterizes the strong northern gradients of geopotential height to be associated with the large-scale thermal-gradient variability that modifies the subtropical jet dynamics and the thermal forcings exerted by low-level cyclonic systems. A further research study was conducted by Colorado-Ruiz and Cavazos[6], who proposed a classification of nine weather patterns for the Mexican region. In analyzing diverse atmospheric datasets, the Self-Organizing Maps clustering technique was employed to discern weather patterns within the Mexican context. They acknowledged that the Self-Organizing Maps clustering technique has limitations in detecting realistic synoptic features associated with extreme events when the spatial domain is very large. However, Colorado-Ruiz and Cavazos's interpretation [6] deviates from the intended meaning, as a spatial domain surpassing that of the interest region is crucial for a comprehensive representation of the extensive synoptic circulation, particularly when the objective is to visualize underlying structures and to identify overall relationships as shown by Ochoa et al. [7] for the study of precipitation over Mexico and surrounding regions. Nevertheless, it is evident that the high local variability of atmospheric variables across the spatial domain may introduce a bias in the SOM training process. Therefore, it is recommended to exclude those high-variability regions to mitigate potential conflicts in the overall interpretation of the results [21]. Furthermore, Gibson et al [34] contend that restricting the spatial domain of the Self-Organizing-Maps clustering algorithm to the regional area would curtail the data's inherent variability and enable the algorithm to encompass less frequent synoptic occurrences within the region. Consequently, smaller and transient circulation features can be more effectively visualized. Spatial constraints are not deemed critical for this research, as the primary objective is to investigate the influence of weather-pattern classification on the Mexican wind field and to elucidate the overarching atmospheric processes that govern wind-field variability and affect wind energy production.

As evidenced in the scientific literature, the definition and quantity of dominant LSWP in Mexico are not well established. This presents an opportunity to investigate not only aspects directly related to LSWP but also how they can modulate the spatial distribution of wind and the variations in energy production. It is evident that the local diurnal variability of wind can be effectively managed through storage and the pliable energy demand. However, significant fluctuations in wind speed, particularly at frequencies beyond the daily scale, pose risks to the uninterrupted operation of economic activities and the overall well-being of the country's inhabitants. In this context, the establishment of informed weather systems that facilitate the recognition of daily weather patterns is crucial for the optimal functioning of wind power systems. Another critical aspect of analyzing Wind Power Systems (WPS) is the statistical modeling of wind speed, singularly at a regional scale. As is well known, wind speed is typically available at a local (spatial/temporal) scale, and its data can be adjusted to the location and hub height of wind turbines using power-law relationships [35]. However, when no information on wind speed is available, reanalysis products provide consistent, long-term, high-resolution velocity fields that can be used to assess WPS [36, 37, 38]. In particular, the ERA5 reanalysis, which is used in this research, is recognized as the best dataset for assessing wind resource patterns over time and space [36].

In the context of this research, we are also interested in investigating which statistical model provides a more accurate description of the wind speed field at the regional scale using the L-moment approach, since it is an efficient technique providing a comprehensive description at the regional scale using the well-known "index-flood" procedure [39, 40]. Furthermore, we explore how these statistical models could assist us in understanding how LSWP modulates potential wind energy fields and in assessing the current Mexican wind power system within the framework of atmospheric synoptic variability. Based on the aforementioned, this manuscript is organized into three main sections. Section 2 describes the source of data that were used for the preceding analyses and the methods for the classification of weather patterns, the statistical inference of the wind speed field in the region of continental Mexico, and the methodology for the estimation of wind power density. Section 3 presents and discusses the results and findings of this research. Finally, section 4 exposes the concluding remarks and highlights the overall interpretation of the obtained results.

2 Methods

2.1 ERA5 Reanalysis

To assess the variability of the wind field surrounding the current Mexico's WPS, we used some of the ERA5 reanalysis atmospheric datasets [41]. These datasets were used to identify and analyze the dynamics of the most prevalent LSWP across Mexico and surrounding regions. Although the ERA5 atmospheric/surface datasets are available globally, this research was conducted primarily to analyze the spatial domain shown in Figure 1; consequently, the ERA5 datasets were trimmed to this domain. As a complementary analysis, two additional spatial domains were incorporated into the study to assess the performance of the clustering approaches with respect to changes in the spatial domain. All three spatial domains are positioned relative to the centroid of the planar surface of Mexico, and the last two domains represent a reduction in areal extent of 75% and 50%, respectively, compared to the domain depicted in Figure 1.

ERA5 datasets that were used in this research are: 1) mean sea level pressure (MSLP), and 2) zonal/meridional wind velocity at 100 meters above the surface (U100/V100). Data are available at a spatial resolution of $0.25° \times 0.25°$ (LON$\times$LAT) and a temporal resolution of 1 hour. However, they were subsequently processed to the daily time scale for the application of the clustering algorithms. To obtain a sub-regional diagnostic of the Mexican wind field over Mexico's WPS, ERA5 wind-velocity datasets were used to extract wind-field information by interpolating the records to the Wind Farms tracked in this study. Currently, approximately 107 wind farms are operational in Mexico. These farms are primarily concentrated in the following regions: Oaxaca (32.7% of the total number of wind farms), Tamaulipas (16.8%), Baja California (9.3%), Yucatán (8.4%), Coahuila (7.5%), Nuevo León (5.6%), Zacatecas (3.7%), Puebla

(3.7%), and a few other regions. For these 107 wind farms, daily time series of zonal/meridional wind velocity and wind speed were compiled for subsequent analysis. It is emphasized that the information on the location and capacity of Mexican wind farms was sourced from the Open Infrastructure Map [42] and The Wind Power [43] web portals.

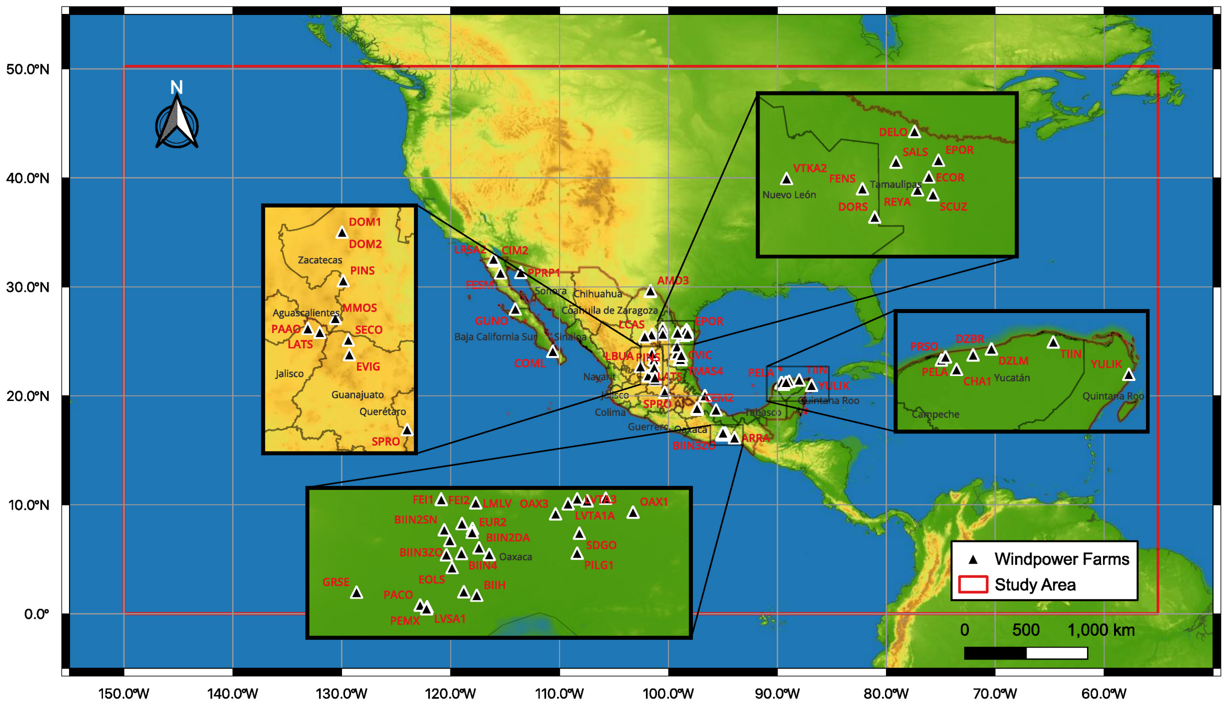

Figure 1: Identification of the spatial domain utilized for the identification of large-scale atmospheric circulation patterns over Mexico's Wind Power System.

To achieve the research objectives, daily MSLP anomalies are used to identify LSWP. As previously mentioned, ERA5 MSLP data originate from their source with a 1-hour time resolution, necessitating post-processing to obtain daily data in the spatial domains SD1, SD2, and SD3 at the original spatial resolution of 0.25 degrees. Daily MSLP anomalies are calculated by first determining the long-term daily mean. The observational period, spanning from January 1, 1940, to December 31, 2024, which serves as the basis for the long-term daily mean. Subsequently, absolute anomalies are derived by subtracting the long-term daily mean from each daily MSLP value. The resulting dataset of MSLP absolute anomalies undergoes linear detrending to yield a suitable study dataset.

As a final step in preparing the MSLP anomalies dataset, a dimensionality-reduction procedure using Empirical Orthogonal Function (EOF) filtering is employed to retain 70% of the explained variance. This procedure reduced the data dimensionality from 76,581 to 7 in the spatial domain SD1, thereby reducing the computational effort required to apply the K-means clustering algorithm. Likewise, the dimensionality of MSLP anomaly fields was also examined in other spatial domains to preserve the same data origin and structure, thereby enabling a fair comparison between the results.

2.2 Clustering Algorithms

Despite extensive and comprehensive developments regarding the application of clustering methods in the context of atmospheric sciences, as evidenced by numerous scientific literature references [15, 21, 12, 34, 24, 25, 7, 44, 11, 10], we will provide technical details regarding the clustering methods employed in this research and the methodology used to determine an appropriate selection of weather patterns.

2.2.1 K-means

The K-means clustering (KMC) algorithm is a data classification technique that partitions the input dataset into a predetermined number K of non-overlapping clusters. Each cluster is characterized by its centroid, which is the arithmetic mean of the fields in the input dataset belonging to that cluster. The classification process entails assigning each input data point to the nearest centroid using Euclidean distance. Furthermore, this process is executed iteratively until the most significant reduction in intra-cluster variance is achieved.

In this research, the KMC algorithm is employed to identify weather patterns based on daily MSLP anomaly fields recorded between January 1, 1940, and December 31, 2024. As mentioned above, the dimensionality of daily MSLP anomaly fields was reduced via EOF filtering to produce a dataset suitable for processing with the KMC algorithm. MATLAB© serves as the software platform for implementing the KMC algorithm, complemented by parallel computing to enhance efficiency.

As suggested by Michelangeli et al. [24], our KMC approach is structured as a dynamic clustering method that compares two pairs of partitions, $P(k)$ and $Q(k)$ (with $k = 1 \dots K$), to assess their similarity. The linear correlation coefficient, denoted as $C(P(k), Q(k))$, and referred to as the anomaly correlation coefficient (ACC), serves as a similarity measure between partitions; consequently, when two partitions are identical, then $C(P(k), Q(k)) = 1$. Michelangeli et al. [24] also recommends testing the dynamical cluster algorithm by comparing all final partitions generated by the algorithm to ensure an optimal clustering. Following their recommendation, the KMC algorithm is initialized independently with $N = 1,000$ random seeds, yielding $1,000$ final partitions, denoted as $P_m(k)$ ($m = 1 \dots N$). The comparison among partitions is conducted using a generalized similarity measure, defined as the classifiability index, which is defined as the average of all ACC values obtained between two distinct partitions within the set of final partitions, specifically, for the partitions $P_i(k)$ and $Q_j(k)$ (with $i \neq j$ and $i, j \in m$), then:

$$\mathrm{CI}\,(k) = \frac{1}{N(N-1)} \sum_{1 \leq i \neq j \leq N} C(P_i(k), Q_j(k)) \tag{1}$$

where, CI (k), or the classifiability index, determines the degree of similarity among all partitions. Moreover, the classifiability index helps infer an appropriate number of clusters for the studied MSLP anomalies dataset. For $k = 1$, the classifiability index CI (k) equals 1, as there is only one distinct way to partition the data into a single pattern. Conversely, for $k > 1$, it is anticipated that the CI (k) will be smaller, as there is a higher likelihood of obtaining different partitions for various iterations of the clustering algorithm when using random-seed initialization. As elucidated by Michelangeli et al. [24] and Agel et al. [15], the most appropriate selection of K is the one that yields the greatest disparity in ACC values obtained between observations and a reference noise model's data. The latter can be obtained by implementing a first-order stationary Markov process that preserves the covariance observed in the EOF-filtered MSLP anomalies dataset. The optimal K value is thus determined by generating 100 samples of the EOF-filtered MSLP anomalies dataset of the same length using the first-order stationary Markov model. For each sample, the CI (k) is computed to obtain an ensemble average of reference-model CI (k), which is subsequently compared with the CI (k) computed for the observations. Consequently, the greater the disparity between observations and the reference noise model, the more reliable the indicator for selecting the optimal value of K becomes.

As a second alternative to determine the optimal number of clusters, the Volume Ratio Index (VRI) is also computed. This index was introduced by Riddle et al. [44] to identify the optimal number of clusters that capture the most significant organizational structures of data. To estimate the VRI, the KMC algorithm must be run sequentially for K values ranging from 1 to 10. For each selected value of K, $N = 1,000$ final partitions should be generated to estimate the cluster radius $R_{i,K}$, for $1 \leq i \leq K$, which is defined as the 90th-percentile distance to the i-centroid. Consequently, the VRI is computed as follows:

$$\mathrm{VRI}\,(K) = \sum_{i=1}^{K} \left(\frac{R_{i,K}}{R_{1,1}} \right)^n \tag{2}$$

where $R_{1,1}$ is the cluster radius of the single cluster (i.e., $K = 1$), assuming a unique organizational structure of data, and n is the dimensionality of the EOF-filtered MSLP anomalies dataset. VRI values are anticipated to be less than unity, as K clusters are more efficient in covering the n-dimensional space of data compared to a single cluster. As suggested by Riddle et al. [44], the first local minimum of the VRI (K) function will be regarded as the optimal number of clusters for representing the organizational structure of data. It is emphasized that to ascertain an objective selection of the optimal number of clusters K, a comparative analysis of results obtained from both methodologies is conducted. The initial objective in employing both methodologies is to derive reference values for K that minimize the subjectivity of the K selection process.

2.2.2 Self-Organizing Maps

The Self-Organizing Maps (SOM) algorithm is a neural network classifier extensively used for the analysis and visualization of atmospheric data arranged in multidimensional space [15, 21, 45, 34, 46, 7]. SOM's objective is to segregate the input data elements into a predetermined discrete topological arrangement of N nodes, thereby reducing data dimensionality. Therefore, nodes in this discrete topological arrangement are employed for pattern recognition, and, under a biological analogy, classification accuracy can be significantly enhanced if the cells are meticulously refined through a competitive learning process [47]. Typically, nodes are organized in a two-dimensional rectangular structure, referred to as the Kohonen layer, to represent the pattern space as weight vectors. In this structure, similar patterns are associated with the nearest nodes through vector quantization (VQ), while less similar patterns are located progressively farther away within the rectangular structure [48, 47].

Vector quantization (VQ) is a technique that generates a continuous probability density function (PDF) $p(\mathbf{x})$ for the input variable $\mathbf{x}$ utilizing a finite set of reference vectors $\mathbf{m}_i$ (with $1 \leq i \leq N$). Once the reference vectors are defined, approximating $\mathbf{x}$ entails identifying the reference vector $\mathbf{m}_c$ that is most closely aligned with $\mathbf{x}$. Typically, the VQ is executed using the Euclidean distance. If the input data are represented by M Euclidean vectors $\mathbf{x}$, and the Kohonen layer is represented by N weight vectors $\mathbf{m}_i$, SOM algorithm aims to minimize the Euclidean distance between the input data and the Kohonen layer weight vectors, i.e., $\|\mathbf{x} - \mathbf{m}_c\| = \arg\min_i\{\|\mathbf{x} - \mathbf{m}_i\|\}$, to identify the Best Matching Unit (BMU) weight vector $\mathbf{m}_c$ and the best partitioning. Therefore, the efficiency of the VQ process can be quantified as follows:

$$E = \int \|\mathbf{x} - \mathbf{m}_c\|^2 \, p(\mathbf{x}) \, d\mathbf{x} \tag{3}$$

where E is an energy function that represents the mean quantization error. Since there is no straightforward definition for $\mathbf{m}_i$, an iterative procedure must be implemented for its estimation. Using the steepest-descent gradient optimization procedure, the reference vector, within the neighborhood radius of the BMU, is updated as follows [49, 47]:

$$\mathbf{m}_i(t+1) = \mathbf{m}_i(t) + \alpha(t) \, h_{ci}(t) \, [\mathbf{x}(t) - \mathbf{m}_i(t)] \tag{4}$$

where $\alpha(t)$ is the learning rate at the iteration t and $h_{ci}(t)$ is the neighborhood function that describes the distance effect on the learning process and plays a crucial role in the self-organization process.

The topology of the Kohonen layer deforms during the minimization process, mainly due to projection errors between the high-dimensional input space and the low-dimensional Kohonen layer. This deformation is quantified using the topographic error (TE), which is formally defined as follows:

$$\text{TE} = \frac{1}{M} \sum_{k=1}^{M} u(\mathbf{x}) \tag{5}$$

where $u(\mathbf{x})$ equals unity if the first nearest weight vector and the second-nearest weight vector are not adjacent, and equals zero if the converse is true. This definition of TE also serves as a measure of the mapping's continuity. Thus, low TE values indicate a high level of topological ordering, implying greater continuity among the classified patterns.

The SOM algorithm is also employed to identify weather patterns in records of daily MSLP anomaly fields. Among the available freeware SOM software, MATLAB's SOM Toolbox 2.0 [50] was used to classify weather patterns. The initial challenge in employing the SOM algorithm lies in determining the optimal dimensionality of the Kohonen layer. The adopted strategy for determining the optimal number of partitions N involved testing various rectangular SOM grid topologies. This involves varying the number of nodes in the lattice spanning from $N = 8$ to $N = 169$. Furthermore, the SOM training process required 10,000 iterations, with a starting learning rate of 0.2 that is linearly reduced to an ending learning rate of 0. The SOM algorithm was trained with a start-point neighborhood radius of 3 that decreases linearly to an end-point neighborhood radius of 1.

Following each iteration of the SOM algorithm, the E and TE values are computed to evaluate the learning and projection quality of the SOM training. As suggested by [21], the dimensionality of the pattern space to be selected is determined by minimizing the root mean squared deviations (RMSD) and the topological distortion of the Sammon map. To achieve a comprehensive and objective selection of the pattern space dimensionality, the RMSD and TE values were normalized to the range 0 to 1. Subsequently, a power function of the form $f(x) = ax^b + c$ was fitted to both the normalized RMSD and TE values to obtain smoothed functions that facilitate visualization of their overall behavior. Thus, by plotting both functions in the same normalized domain, the intersection point provides insight into the optimal number of nodes that minimizes the RMSD while ensuring that the topological distortion of the pattern space is not exceeded.

Finally, we highlight that the degree of similarity between the SOM's patterns (or spatial representations of Kohonen layer weight vectors) and the observed daily MSLP is ultimately determined by a pattern correlation measure, as suggested by [34]. Consequently, the daily distribution of weather patterns is estimated through Pearson-type correlation analysis between the SOM patterns and daily MSLP fields. This analysis serves as a basis for classifying wind-speed data groups and subsequently estimating their probability distribution parameters.

2.3 Regional Analysis of Wind Speed

As evidenced by numerous studies, the Weibull distribution is extensively employed to characterize the frequency distribution of wind speed data [51, 35, 52, 53, 54, 55, 56, 57, 58, 59], since it can provide valuable insights into the regional variability of the wind speed field, encompassing factors such as altitude, seasonality, and persistence. As is known, the Weibull distribution parameters facilitate the estimation of maximum wind speed and the average power density. However, estimating Weibull distribution parameters is subject to various sources of uncertainty; therefore, different approaches have been studied and compared to obtain suitable estimates. To overcome the hurdles identified in prior studies on the endorsement and analysis of the Weibull distribution for characterizing wind speed at the regional scale, the L-moment ratio approach is explored here to obtain a suitable statistical description of Mexico's wind speed field. In the Appendix section, some formal concepts pertaining to the theory of L-moments are introduced, which can be disregarded by instructed readers on this theory.

The theory of L-moment ratios was introduced by [39, 40] as a method for estimating the parameters of probability distributions and its application to the regional frequency analysis. Furthermore, this theory presents an approach that minimizes the need to identify the distribution that best characterizes the observations across various families (e.g., Weibull, Generalized Extreme Value (GEV), Generalized Pareto (GPD), Generalized Logistic (GLO), Exponential, Gumbel, Kappa).

In this study, the theory of L-moment ratios is used to estimate distribution parameters, which are fitted to continental wind speed data over Mexico for the period from 1940 to 2024. To facilitate the analysis of the distributions and the selection of the optimal model for Mexico's wind speed field, the L-moment ratio diagrams have been employed. These diagrams serve as graphical representations of the relationships among the L-moment ratios, facilitating the comparison of empirical L-moment ratios with those predicted by theoretical relationships for selected distributions, and providing insight into the overall statistical structure of the data.

To conduct a regional frequency analysis utilizing ERA5 wind speed records over Mexico's continental region, a homogeneous dataset is essential. Consequently, the "index-flood" procedure, as introduced by Hosking and Wallis [40], was employed on our data to derive the most representative sample data that meet the homogeneity criterion. If there are N_s elements of the wind speed field recorded over Mexico's continental region, and each element i has a sample U_i of wind speed data in the period spanning from 1940 to 2024, we will select those sample data that form a homogeneous region. This means that there is a unique normalized frequency distribution representative of the m-wind-speed samples that can be modulated for local frequency analysis by a site-specific scaling factor. This is:

$$x_i(F) = \mu_i \, y_i(F) \tag{6}$$

where $x_i(F)$ represents the quantile function of the probability distribution of wind speed at site i, μ_i denotes the site-specific scaling factor, which is equivalent to the mean of the sample data at location i, and $y_i(F)$ is the regional dimensionless quantile function, commonly referred to as the regional growth curve.

Hosking and Wallis [40] suggest checking the homogeneity criterion by using a heterogeneity measure, after disregarding the discordant sample data of the regional analysis. If each sample data is characterized by the L-moment ratios $\mathbf{a}_i = [\tau^{(i)}, \tau_3^{(i)}, \tau_4^{(i)}]^T$, with $i = 1 \ldots N_s$ the group average of L-moment ratios is defined as $\bar{\mathbf{a}} = N_s^{-1} \sum_i^{N_s} \mathbf{a}_i$, and the discordancy measure for the sample data i is given by:

$$D_i = \frac{1}{3} N_s (\mathbf{a}_i - \bar{\mathbf{a}})^T \mathbf{A}^{-1} (\mathbf{a}_i - \bar{\mathbf{a}}) \tag{7}$$

where,

$$\mathbf{A} = \sum_{i=1}^{N_s} (\mathbf{a}_i - \bar{\mathbf{a}})(\mathbf{a}_i - \bar{\mathbf{a}})^T \tag{8}$$

Discordant data are identified as those with $D_i \geq 3$. After excluding these discordant data from the homogeneous region, the regional average L-moment ratios τ^R, τ_3^R, and τ_4^R are estimated. Consequently, the heterogeneity measure is calculated as:

$$H = \frac{V - \mu_V}{\sigma_v} \tag{9}$$

where, V represents the standard deviation of the sample L-CV, μ_V and σ_v denote the mean and standard deviation of N_{sim} values of V, respectively. If $H < 1$, the conformed region is deemed acceptably homogeneous. Finally, the degree of goodness-of-fitting of the regional probability distribution is estimated using the following quantity [40]:

$$Z^{\text{D}} = \frac{\tau_4^{\text{D}} - \tau_4^{\text{R}} + B_4}{\sigma_4} \tag{10}$$

where, τ_4^{R} and τ_4^{D} represent the regional and distribution L-kurtosis, respectively; σ_4 is the regional standard deviation of τ_4^{R}, and B_4 is the average bias of τ_4^{R}. If $|Z^{\mathrm{D}}| \leq 1.64$ the fitting to the test probability distribution is considered adequate for a confidence level of 90%. As previously mentioned, the Weibull distribution is primarily regarded as the initial candidate distribution for the regional description of wind speed over continental Mexico. Nevertheless, as an alternative probability distribution, the four-parameter Kappa distribution is also considered to describe the wind speed field. In the Appendix, further details on the Kappa distribution function are provided as complementary information to that presented herein.

As part of the statistical analysis of wind speed, the comparison among distributions characterizing prevailing weather patterns is assessed using the Kullback-Leibler divergence. This measure, originating from information theory, quantifies the dissimilarity between two probability distributions. If the probability distribution of the wind velocity field associated with weather pattern i is denoted by $F_i(x)$, the dissimilarity between every pair of distributions is determined as follows:

$$D_{\mathrm{KL}}(F_i||F_j) = \int_0^{\infty} f_i(x)\, \log\left(\frac{f_i(x)}{f_j(x)}\right) dx \tag{11}$$

The main properties of the KL divergence measure are as follows: 1) it is always positive: $D_{\mathrm{KL}}(F_i||F_j) \geq 0$; 2) it is asymmetric: $D_{\mathrm{KL}}(F_i||F_j) \neq D_{\mathrm{KL}}(F_j||F_i)$, making it unsuitable as a regular distance metric; 3) if X and Y are independent and identically distributed random variables, the additivity property holds: $D_{\mathrm{KL}}(F_{X,Y}||Q_{X,Y}) = D_{\mathrm{KL}}(F_X||Q_X) + D_{\mathrm{KL}}(F_Y||Q_Y)$.

2.4 Wind Energy Assessment

A primary goal of this research is to examine the influence of LSWP variability on the potential wind energy fields over Mexico. Therefore, wind power density and maximum energy production are used to quantify available wind energy resources and how they are modulated by the dominant LSWP. Wind power density is defined as the energy available per unit of time and rotor cross-sectional area at a specific location for the conversion of wind energy into electricity [35], which is approximated by:

$$P_d(u) = \frac{1}{2}\rho \int_0^{\infty} u^3\, f(u)\, du \qquad [\,\mathrm{W\,m^{-2}}\,] \tag{12}$$

where ρ is the air density, and $f(u)$ is the selected probability density function that models the wind speed field over Mexico. Given that the ERA5 wind speed records were obtained at a height of 100 meters, the density (ρ) values were estimated at the same height using appropriate ERA5 atmospheric products and vertical interpolations for this purpose.

The second significant variable for the wind energy assessment is the wind speed associated with the maximum energy production. Since the function $u^3\, f(u)$ reach a maximum value at some wind speed u_{me}, the maximum energy production $W_{\max}$ obtained during a period T, in hours, is estimated as follows:

$$W_{\max} = \frac{1}{2}\rho\, u_{me}^3\, f(u_{me})\, T \qquad [\mathrm{W\,h\,m^{-2}}] \tag{13}$$

where u_{me} denotes the speed that generates the most energy, which is also regarded as the rated wind speed for turbine designs [35]. Within the framework of this research, wind power density and maximum energy production were estimated at regional scales for continental Mexico. Furthermore, to estimate maximum energy production, the period T is taken as the sum of the average number of hours per year when the weather patterns occur.

3 Results and Discussion

3.1 Identification of LSWP

3.1.1 KMC Classification

As previously mentioned, the initial critical element in the development of this research is the identification of LSWP that characterizes and simplifies the overall dynamical states of the atmosphere. Two clustering techniques were employed for this purpose, and their findings will be presented in this section.

The initial analysis involves determining the most representative number of weather patterns for the study region. Employing the K-means clustering technique and the largest domain, designated as SD1, four LSWP are proposed as characteristics of Mexico and its surrounding regions. Figure 2 illustrates the classifiability index (CI) and the volume ratio index (VRI) as a function of the number of clusters, K, for a K-means clustering analysis of the daily MSLP anomalies on the spatial domain SD1. Both functions were estimated for K values ranging from 2 to 10. The confidence interval for each classifiability-index plot is estimated using the 10th and 90th percentiles of the confidence intervals obtained from 100 samples drawn from the reference model data. Similarly, the confidence interval of each volume-ratio-index plot is determined by the 10th and 90th percentiles of the VRI values derived from 1,000 random partitions of the K-means clustering outputs.

Either the CI or the VRI function shows a decreasing trend as K-values increase. The highest value of CI is consistently observed at $K = 2$, signifying that the anomaly correlation coefficient (ACC) between centroids of distinct partitions is predominantly one, implying that the centroids are identical. As observed in Figure 2, the CI-function of the reference model exhibits an abatement as the number of clusters, K, increases, which means that the centroids of different partitions become distinct as the number K increases. Similarly, the CI-function of the observations (i.e., the EOFs of daily MSLP anomalies) exhibits abatement behavior analogous to that of the reference model. However, its rapid abatement starts at $K = 4$, rather than $K = 3$ for the reference model. Since there is a significant difference between the classifiability-index values obtained from observations and those of the reference model at $K = 4$, this suggests that the optimal number of LSWP for the spatial domain SD1 is four. Likewise, the VRI function indicates that $K = 4$ is the most suitable choice for the number of clusters, as its initial local minimum is located at $K = 4$. Furthermore, for $K > 4$, the VRI function approaches 0.3, suggesting that clusters obtained by the K-means clustering algorithm contain a comparable number of elements that remain unchanged across organizational datasets. Hence, the initial local minimum of the VRI function yields a unique solution for selecting $K = 4$.

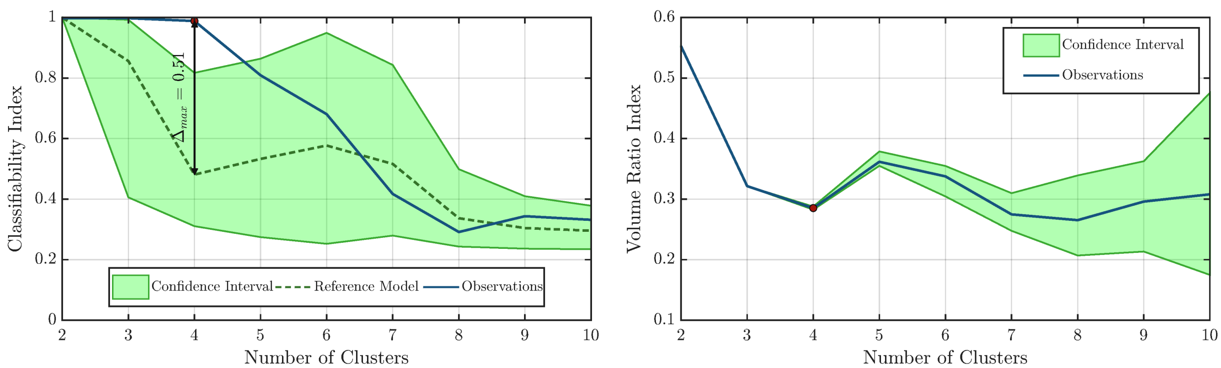

Figure 2: Identification of the optimal number of clusters using the KMC algorithm. The left plot displays the Classifiability Index (CI) for each partition K ranging from 2 to 10. The right plot presents the Volume Ratio Index (VRI) for the same range of partition values. The green shaded region in the Classifiability Index represents the 90% confidence interval for the reference model's results. In the same way, the confidence interval of the Volume Ratio Index represents the 90% confidence interval of the mean obtained from 1,000 iterations of the KMC algorithm.

Similarly, the analysis to identify the optimal number of LSWP was conducted for two smaller domains. In the second spatial domain (domain reduced in area by 75%), there is no equivalence among the estimations of the optimal number of clusters obtained from both indices. The largest significant difference in CI values between observations and the reference model occurs at $K = 9$, and the VRI function exhibits invariability at $K \geq 5$. This indicates that reducing the original domain enhances the complexity of LSWP identification. This is because smaller spatial features gain prominence during classification and become challenging to represent within a data organization structure with a limited number of atmospheric states. The analysis conducted for the third spatial domain (domain reduced in area by 50%) strengthens the hypothesis that smaller spatial features may introduce inconsistencies in the definition of the optimal number of LSWP. For the third spatial domain, the largest significant difference in CI values between observations and the reference model occurs at $K = 5$, and the VRI function is invariant for $K \geq 6$.

Upon conducting a comprehensive analysis of the CI and VRI functions, our results suggest that the optimal number of LSWP is $K = 4$ for the original spatial domain, $K = 5$ for the second domain, and $K = 6$ for the third domain. These findings show that dimensional changes in the spatial domain influence the decision-making process for selecting the optimal partition that most effectively captures the most prevalent atmospheric weather patterns. Furthermore, our results indicate that as the spatial domain becomes smaller, the number of LSWP required to accurately represent the data organizational structure increases. Since that for an overall representation of the LSWP of Mexico and surrounding regions, a unique number of clusters and a spatial domain would be necessary. To identify extensive synoptic structures that may modify the large-scale circulation wind-field patterns and the local production of wind energy, $K = 4$ is selected under the principle of Occam's razor (i.e., fewest assumptions for solving the problem). This selection is supported by the fact that the organizational structure of the four LSWP can be discerned across all spatial domains, with subtle variations in the representation of certain wind-field features.

The overall portrayal of the four LSWP in terms of the compound wind field can be observed in Figure 3. The pattern WP_1 is characterized by a high-pressure system over the western continental United States and the northern subtropical Pacific, with a trough along the east coast of Mexico, extending from the Gulf of California. This pattern illustrates the North Pacific Subtropical High (NPSH), which maintains dry weather conditions over the western United States and the trade winds. Furthermore, the strong high-pressure system over the southeastern United States indicates a blocking-high pattern responsible for regional heat waves.

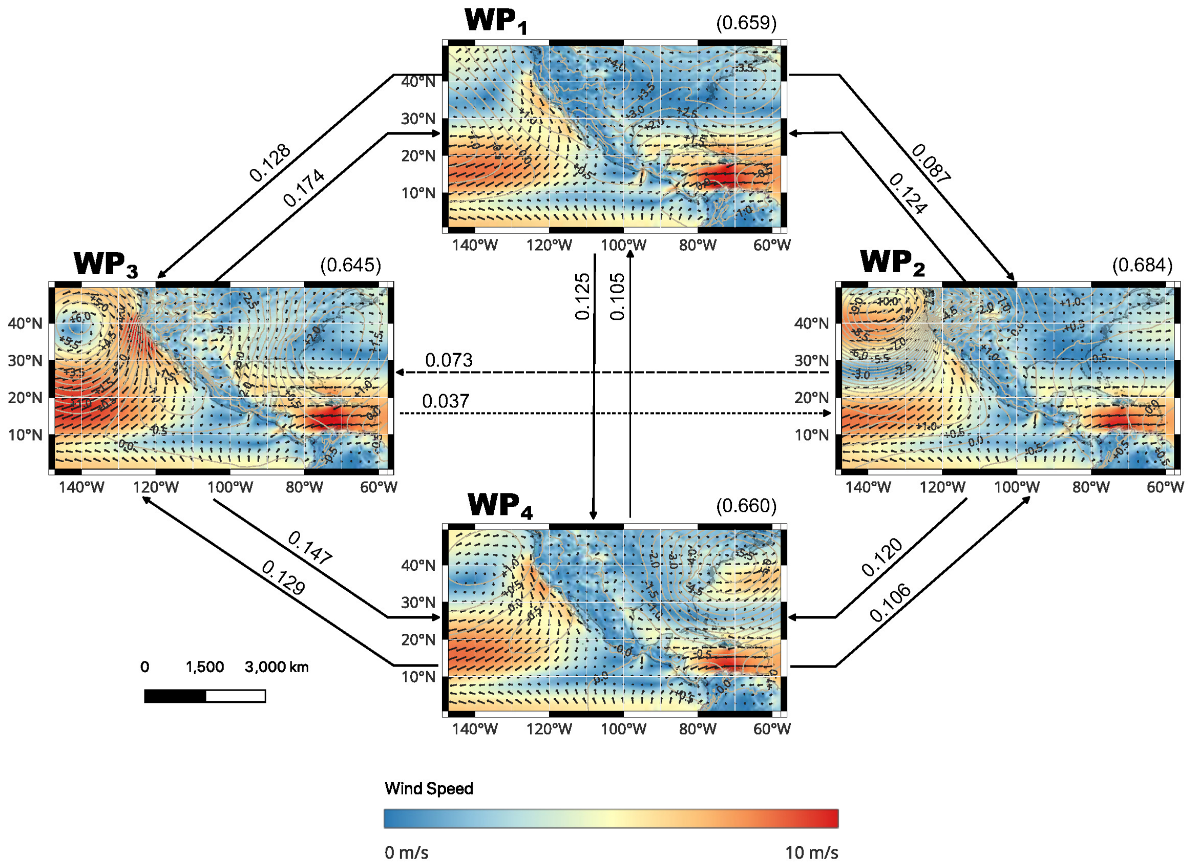

Figure 3: Wind velocity patterns at a height of 100 meters, as determined by the KMC algorithm. The (composite) wind velocity patterns (WP_j) were computed by considering the days of occurrence of the MSLP anomaly fields within the historical record. Those wind velocity fields that were classified as belonging to the cluster j are averaged to obtain the pattern WP_j. All the plots illustrate wind velocity vectors and their corresponding wind speed fields, accompanied by isolines of pressure anomaly (dashed lines). Furthermore, the transition probabilities between wind velocity patterns are shown above the arrow lines connecting the patterns.

The pattern WP_2 exhibits a low-pressure system in the Pacific Northwest and is recognized as a significant weather driver responsible for cool, wet, widespread clouds and windy conditions during the fall and boreal winter months along the western coast of the United States. During this low-pressure system, the NPSH weakens and is displaced southward; consequently, the air that circulates around the low-pressure system and the NPSH moves eastward, conveying moisture to the northeastern inland area of the United States. Additionally, the surface wind that flows over the NPSH is deflected southeast over the Gulf of California, where it slows. In the northeastern United States, an extended high-pressure system is also observed in the second LSWP. This system appears to enhance the wind speed around the Isthmus of Tehuantepec.

The pattern WP_3 exhibits a trough pattern characterized by the presence of two high-pressure circulation systems: the North Pacific Subtropical High (NPSH) and the North Atlantic Subtropical High (NASH). The NPSH within WP_3 appears to be more intense than that observed in the other LSWP, leading to the intensification of upwelling alongshore surface winds in the western coasts of the United States [60] and the low-level equatorward flow along the west of the

Baja California Peninsula [5, 61]. Moreover, the amplification of the NASH enhances wind flow over the Tamaulipas region and the coastal trade winds entering the Gulf of Mexico.

The pattern WP_4 shows a weaker condition of the NPSH, which is slightly displaced southward. The airflow surrounding this circulation system is characterized by a swift motion over the coastal regions of North and South Baja California. The pattern WP_4 also exhibits a low-pressure system situated in the northeastern United States, which enhances the surface wind speed within this circulation system in the oceanic region. Furthermore, this weather pattern is associated with a positive-tilted trough that extends from the low-pressure system in the northeast to the continental United States in a southwest direction. WP_4 appears to be the dominant atmospheric condition during winter, exerting a significant influence on wind speed in the vicinity of the Isthmus of Tehuantepec and surrounding regions.

Following Vautard et al.'s suggestion [62] regarding the description of the communication flow of LSWP, a transitional description based on Markov chains would be appropriate for this purpose. As illustrated in Figure 3, the communication flow among the four LSWP is represented by a set of solid-line arrows that delineate the transition directionality among the LSWP (i.e., $\mathrm{WP}_i \to \mathrm{WP}_j$) and above these arrows, the transition probability (i.e., $p_{ij} = \Pr\{\mathrm{WP}_j \mid \mathrm{WP}_i\}$) is presented. Furthermore, the number situated in the upper-right corner of each plot indicates the transition probability of maintaining the same state (i.e., $p_{jj} = \Pr\{\mathrm{WP}_j \mid \mathrm{WP}_j\}$). The transition probabilities were estimated by counting the frequency of pattern WP_i switching to pattern WP_j on a daily timescale. The transition probability matrix, also known as the stochastic matrix, for the KMC classification of the four LSWP is presented below:

$$p_{ij} = \begin{array}{c c} & \begin{array}{cccc} 1 & 2 & 3 & 4 \end{array} \\ \begin{array}{c} 1 \\ 2 \\ 3 \\ 4 \end{array} & \begin{Vmatrix} 0.659 & 0.087 & 0.128 & 0.125 \\ 0.124 & 0.684 & 0.073 & 0.120 \\ 0.171 & 0.037 & 0.645 & 0.147 \\ 0.105 & 0.106 & 0.129 & 0.660 \end{Vmatrix} \end{array} \tag{14}$$

The significance of these transition probabilities was evaluated using a Monte Carlo simulation framework, which enabled the computation of the p-values for each element of the stochastic matrix. Consequently, for a significance level of $\alpha = 0.10$, all the transition probabilities of the stochastic matrix are significant. Based on the properties of the stochastic matrix, shown in Equation 14, the transitions among LSWP can be represented as an irreducible and aperiodic Markov chain, whose stationary distribution is given by:

$$\pi = \begin{array}{c} \begin{array}{cccc} 1 & 2 & 3 & 4 \end{array} \\ \begin{bmatrix} 0.280 & 0.199 & 0.243 & 0.278 \end{bmatrix} \end{array} \tag{15}$$

Furthermore, its spectral properties indicate a faster convergence of the Markov chain to its stationary distribution, as seen in its relaxation time of $\tau \approx 3$ days. Another property to highlight from this Markov chain is the mean first passage matrix, which represents the expected number of steps (measured in days) that the Markov chain takes to reach state WP_j for the first time, starting from state WP_i. Upon inspection of the mean first-passage matrix, the four LSWP identified by the KMC algorithm are recurrent states with an average recurrence time of approximately four days, indicating a potential occurrence frequency of twice per month. Notably, transitions towards the state WP_2 are characterized by a longer duration, suggesting a reduced likelihood of such transitions. These last results show that there are expeditious transitional dynamics among weather patterns, suggesting that the temporal classification of weather-pattern occurrences obtained via the KMC algorithm is improper compared with observational evidence.

3.1.2 SOM Classification

As previously mentioned in the methodology section, the SOM algorithm is applied to identify LSWP over Mexico and surrounding regions using an ERA5 dataset of daily MSLP anomalies. Similar to the KMC technique, SOM requires prior knowledge of the number of LSWP to be identified. Consequently, the assessment of the number of LSWP, also known as the number of map nodes, was conducted in an innovative way. The conventional practice recommends employing the elbow criterion to the error function (e.g., quantization error, topographic error, etc.) as a function of the number of map nodes. The location of a quasi-inflection point in the error function indicates substantial variation in the function and, predominantly, the presence of an excessive number of nodes that do not contribute to the pattern recognition process. In this research, the root mean squared deviation (RMSD) and topographic error (TE) functions were normalized and plotted over the same data domain to identify the point where RMSD is minimized while minimizing topographic error. As illustrated in Figure 4, the RMSD data exhibits a decaying trend, which can be effectively modeled by a power function. Conversely, the TE data show a growing trend, maintaining a relatively stable trajectory around TE≈ 0.8 for more than 18 nodes. The intersection point between the smoothed error functions, located at approximately 16 nodes, suggests the existence of a map with a node count that enables a reduction of approximately 50% in the RMSD without exceeding a 50% increase in the TE. As depicted in Figure 4, the map constructed using 15 nodes is deemed to have achieved a sufficiently reduced RMSD without surpassing a topographic error of 50%.

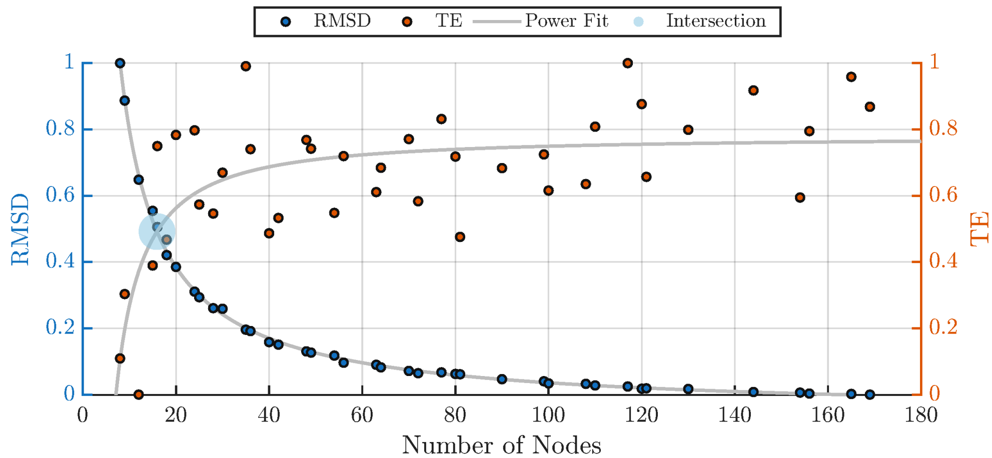

Figure 4: Normalized values of Root Mean Squared Difference (RMSD) and Topographic Error (TE), which were estimated for various topological configurations of the Kohonen layer. These metrics were applied to daily MSLP anomaly data spanning from 1940 to 2024.

Based on the results observed in Figure 4, the map comprising 15 nodes is considered the most suitable choice for the original spatial domain. It is highlighted that the decay and growth rates of the error functions, RMSD, and TE are influenced by the spatial domain size. Specifically, the smaller the spatial domain size, the higher the TE growth rate. Besides, the intersection point between both error functions indicates a higher number of nodes in comparison to that of the original spatial domain. Similar to the analysis conducted using the KMC algorithm, these findings indicate that the SOM classification of weather patterns becomes more intricate as the domain extent decreases. This is attributed to the increased complexity in accurately representing the variability of local spatial features and ensuring the topological continuity of the patterns within the maps.

Analogous to the visual representation of the LSWP identified by the KMC algorithm, Figure 5 illustrates the 15 LSWP discovered by the SOM algorithm. Evidently, the diversity of patterns is greater than that obtained by the KMC algorithm. Nevertheless, certain similarities in the wind field can be discerned in weather patterns that exhibit a spatial structure comparable to the composite daily MSLP anomalies and wind field. Specifically, the weather patterns WP_7, WP_4, WP_3 and WP_9 obtained using the SOM algorithm exhibit high spatial correlation and geometric similarity with the weather patterns WP_1, WP_2, WP_3 and WP_4, obtained using the KMC algorithm. The fact that the SOM algorithm can identify weather patterns that the KMC algorithm has discovered underscores its superior ability to depict synoptic processes and reproduce results achieved by other techniques.

We remark that the KMC algorithm enables the classification of weather patterns without considering their interconnections. However, once observations are allocated based on the minimal Euclidean distance to the centroid, the resulting stochastic matrix establishes a probabilistic connectivity among the weather patterns. Conversely, the SOM algorithm offers an advantage over the KMC algorithm by organizing weather patterns using the neighborhood function and regulating communication among them. In this regard, the SOM weather patterns highlight the transitions among them, providing a more comprehensive description of spatial variations in the wind field, encompassing both the intensity and directionality of local wind velocity. Furthermore, SOM offers more expedient control over the physical processes that may occur as weather patterns evolve.

As illustrated in Figure 5, the SOM weather patterns depict synoptic changes primarily associated with the interactions between the high-pressure circulation systems NPSH and NASH. Beginning with WP_1, this weather pattern exhibits a trough pattern where the two anticyclonic circulation systems, NPSH and NASH, form a saddle point over the continental region of Mexico. This atmospheric configuration is characterized by weak pressure gradients and a calm wind field over inland Mexico. As the NPSH intensifies, the high-pressure center shifts northward, as observed in patterns WP_2 and WP_3, and the wind speed intensifies along the western Baja California peninsula. Furthermore, the attenuation and eastward displacement of the NASH reduce the incoming wind flow that enters the inland region over Tamaulipas and the southeastern United States.

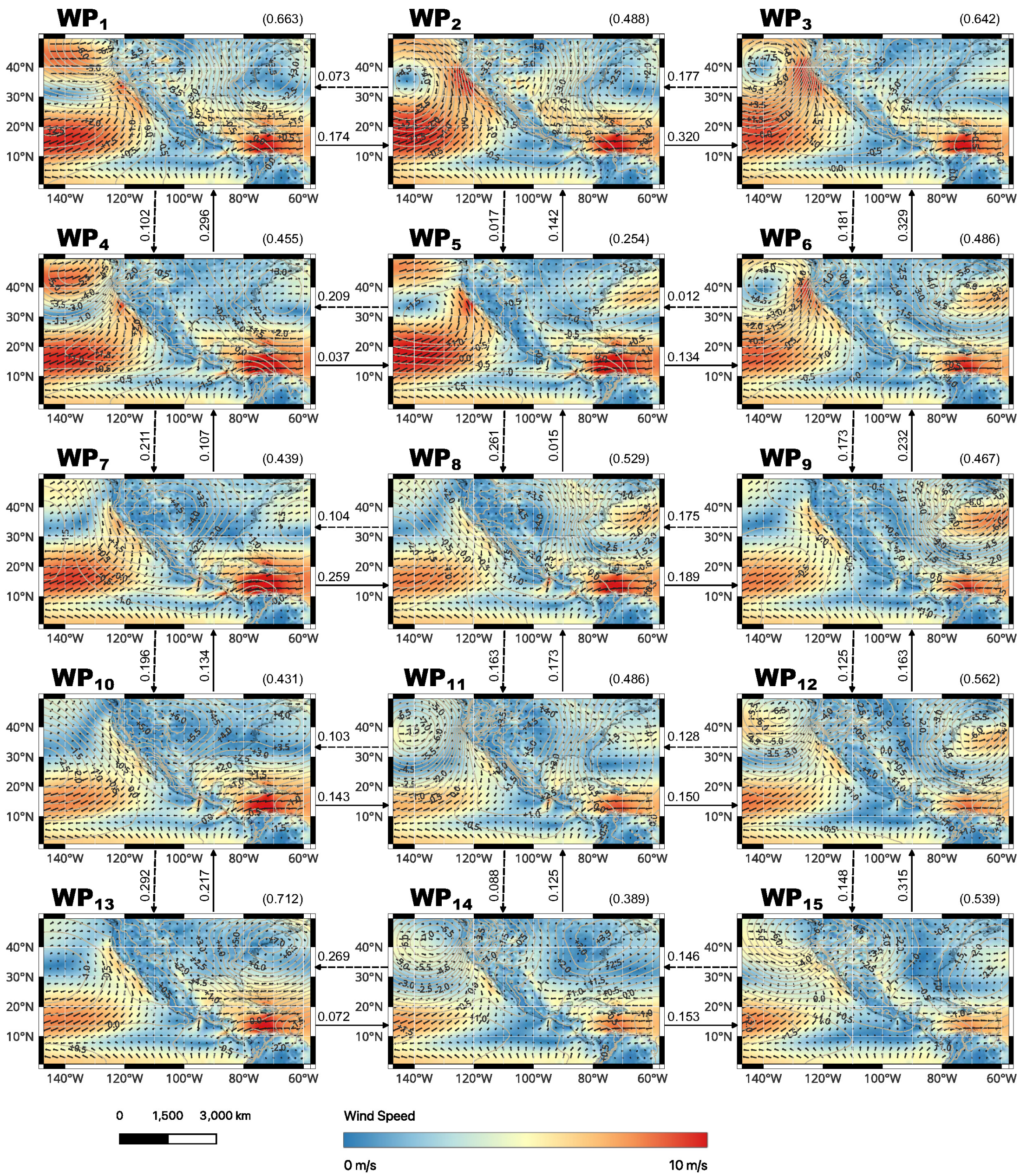

Figure 5: Wind velocity patterns at 100 m, as determined by the SOM algorithm for a 3×5-nodes topology map. The (composite) wind velocity patterns (WP_j) were computed by considering the days of occurrence of the MSLP anomaly fields within the historical record. Those wind velocity fields that were classified as belonging to the cluster j are averaged to obtain the pattern WP_j. All the plots illustrate wind velocity vectors and their corresponding wind speed fields, accompanied by isolines of pressure anomaly (dashed lines). Furthermore, the transition probabilities between wind velocity patterns are shown above the arrow lines connecting the patterns.

The emergence of a low-pressure circulation system over the northeastern United States region, as observed in the patterns WP_6, WP_9, and WP_{12}, enhances the westerly wind flow over the Atlantic Ocean at latitudes 30° to 40°. Additionally, this low-pressure circulation system appears to modulate the intensification of the wind flow over the Isthmus of Tehuantepec and the entrance flow over the region of Tamaulipas. As this system weakens, as shown in WP_{15}, the most significant reduction in wind speed over the Isthmus of Tehuantepec is observed, highlighting this weather pattern as the most critical for wind energy production in southern Mexico, particularly in Oaxaca and Chiapas. Conversely, the intensification of a continental high-pressure system, as evidenced over the inland central United States region and observed in the patterns WP_7, WP_{10}, and WP_{13}, results in an augmentation of the wind flow over the Isthmus of Tehuantepec.

As previously mentioned, the SOM algorithm may provide a more comprehensive description of feasible scenarios for the LSWP and the interconnections among these weather patterns. Figure 5 illustrates the communication between weather patterns, using (solid/dashed) line arrows to establish connections. The numerical value above each line arrow represents the transition probability between the respective weather patterns $p_{ij} = \Pr\{\mathrm{WP}_j \,|\, \mathrm{WP}_i\}$. Moreover, the value shown in the upper-right corner of each plot represents the transition probability $p_{ii} = \Pr\{\mathrm{WP}_i \,|\, \mathrm{WP}_i\}$. In accordance with the weather-patterns communication arrangement depicted in Figure 5, the resulting stochastic matrix is presented in Equation 16. This matrix was estimated in a manner analogous to that used to compute the KMC stochastic matrix, but accounting for the SOM map topology and its inherent interconnections among weather patterns. Furthermore, employing a Monte Carlo simulation framework enabled the determination of the significance of the transition probabilities. Notably, for $\alpha = 0.1$, all transition probabilities are significant.

$$p_{ij} = \begin{array}{r|ccccccccccccccc|}
 & 1 & 2 & 3 & 4 & 5 & 6 & 7 & 8 & 9 & 10 & 11 & 12 & 13 & 14 & 15 \\
1 & 0.663 & 0.235 & 0.000 & 0.102 & 0.000 & 0.000 & 0.000 & 0.000 & 0.000 & 0.000 & 0.000 & 0.000 & 0.000 & 0.000 & 0.000 \\
2 & 0.174 & 0.488 & 0.320 & 0.000 & 0.017 & 0.000 & 0.000 & 0.000 & 0.000 & 0.000 & 0.000 & 0.000 & 0.000 & 0.000 & 0.000 \\
3 & 0.000 & 0.177 & 0.642 & 0.000 & 0.000 & 0.181 & 0.000 & 0.000 & 0.000 & 0.000 & 0.000 & 0.000 & 0.000 & 0.000 & 0.000 \\
4 & 0.296 & 0.000 & 0.000 & 0.455 & 0.037 & 0.000 & 0.211 & 0.000 & 0.000 & 0.000 & 0.000 & 0.000 & 0.000 & 0.000 & 0.000 \\
5 & 0.000 & 0.142 & 0.000 & 0.209 & 0.254 & 0.134 & 0.000 & 0.261 & 0.000 & 0.000 & 0.000 & 0.000 & 0.000 & 0.000 & 0.000 \\
6 & 0.000 & 0.000 & 0.329 & 0.000 & 0.012 & 0.486 & 0.000 & 0.000 & 0.173 & 0.000 & 0.000 & 0.000 & 0.000 & 0.000 & 0.000 \\
7 & 0.000 & 0.000 & 0.000 & 0.107 & 0.000 & 0.000 & 0.439 & 0.259 & 0.000 & 0.196 & 0.000 & 0.000 & 0.000 & 0.000 & 0.000 \\
8 & 0.000 & 0.000 & 0.000 & 0.000 & 0.015 & 0.000 & 0.104 & 0.529 & 0.189 & 0.000 & 0.163 & 0.000 & 0.000 & 0.000 & 0.000 \\
9 & 0.000 & 0.000 & 0.000 & 0.000 & 0.000 & 0.232 & 0.000 & 0.175 & 0.467 & 0.000 & 0.000 & 0.125 & 0.000 & 0.000 & 0.000 \\
10 & 0.000 & 0.000 & 0.000 & 0.000 & 0.000 & 0.000 & 0.134 & 0.000 & 0.000 & 0.431 & 0.143 & 0.000 & 0.292 & 0.000 & 0.000 \\
11 & 0.000 & 0.000 & 0.000 & 0.000 & 0.000 & 0.000 & 0.000 & 0.173 & 0.000 & 0.103 & 0.486 & 0.150 & 0.000 & 0.088 & 0.000 \\
12 & 0.000 & 0.000 & 0.000 & 0.000 & 0.000 & 0.000 & 0.000 & 0.000 & 0.163 & 0.000 & 0.128 & 0.562 & 0.000 & 0.000 & 0.148 \\
13 & 0.000 & 0.000 & 0.000 & 0.000 & 0.000 & 0.000 & 0.000 & 0.000 & 0.000 & 0.217 & 0.000 & 0.000 & 0.712 & 0.072 & 0.000 \\
14 & 0.000 & 0.000 & 0.000 & 0.000 & 0.000 & 0.000 & 0.000 & 0.000 & 0.000 & 0.000 & 0.189 & 0.000 & 0.269 & 0.389 & 0.153 \\
15 & 0.000 & 0.000 & 0.000 & 0.000 & 0.000 & 0.000 & 0.000 & 0.000 & 0.000 & 0.000 & 0.000 & 0.315 & 0.000 & 0.146 & 0.539
\end{array} \tag{16}$$

Among the properties of the stochastic matrix derived from the SOM-classified LSWP, it is highlighted that it can be characterized as an irreducible and aperiodic Markov chain with a stationary distribution given by:

$$\begin{array}{rccccccccccccccc}
 & 1 & 2 & 3 & 4 & 5 & 6 & 7 & 8 & 9 & 10 & 11 & 12 & 13 & 14 & 15 \\
\pi = & [0.069 & 0.095 & 0.179 & 0.023 & 0.007 & 0.102 & 0.036 & 0.079 & 0.082 & 0.055 & 0.067 & 0.068 & 0.081 & 0.027 & 0.031]
\end{array} \tag{17}$$

This distribution suggests that the most probable weather pattern to occur is WP_3, which is characterized by the highest intensification and northward displacement of the NPSH. Conversely, the less likely weather pattern to occur is characterized by a highly intensified and southward-shifted NPSH, in conjunction with an attenuated eastward-shifted NASH. In contrast to the rapid convergence exhibited by the stationary distribution of the KMC weather patterns, the stationary distribution of the SOM weather patterns exhibits a longer relaxation time of approximately $\tau = 7$ days, which means a slow convergence to the stationary distribution. The first passage matrix for the SOM-classified LSWP enables us to show that all weather patterns are recurrent states with an average recurrence period of approximately 28 days. Notably, the weather pattern with the lowest probability of occurrence exhibits the longest recurrence time (i.e., $\mu_{55} = 150$ days), while the weather pattern with the highest probability of occurrence exhibits the shortest recurrence time (i.e., $\mu_{33} = 5$ days). These findings emphasize that the dominance of intensified NPSH and the synchronic action of NASH are characteristic conditions in the study region. Under these conditions, moderate easterly winds are anticipated to enter the Tamaulipas region, strong winds are expected over the western coast of Baja California's Peninsula, and a moderate southward wind is anticipated to exit from the Isthmus of Tehuantepec.

This investigation identified large-scale weather patterns spanning Mexico and neighboring regions, necessitating an examination of two widely recognized techniques for clustering and pattern recognition. These techniques establish a coherent correlation with the structural characteristics of synoptic patterns that govern the Atlantic and Pacific oceans. Despite our findings indicating the prevalence of 15 large-scale weather patterns within the study region, it is noteworthy that the interactive and interdependent nature of the two high-pressure systems in both oceans could diversify weather patterns. This diversification of patterns can either enhance or diminish the wind field over time; furthermore, it can lead to strong fluctuations in wind energy generation.

3.2 Regional Wind Speed Distribution

As noted above, the regional analysis of the wind speed field was conducted using selected data from the continental region of Mexico, spanning 1940 to 2024. These data were analyzed using the theory of L-moment ratios, which serve as the primary statistical framework for selecting a regional wind speed distribution and estimating quantiles. Approximately $N_s = 13,064$ spatial data points constitute the continental region of Mexico, which collectively describe the spatial variability of the wind speed field. Additionally, $m = 31,047$ temporal data points represent the duration of daily wind speed records at each spatial data point. Given that the primary objective of the statistical analysis is to derive a statistical description of the wind field based on the variability of weather patterns, a top-down approach is employed. This approach entails segregating wind speed data by the occurrence of each weather pattern. In that regard, the allocation vector of weather patterns that results from the application of a similarity measure between the records and the set of weather patterns derived by SOM algorithms is used to form a partition $Q = \{q_1, q_2, \ldots, q_N\}$ of the wind speed dataset X, such that Q is equipped with the properties: 1) $\emptyset \notin Q$, 2) $X = \bigcup_{i=1}^{N} q_i$, and 3) $q_i \bigcap q_j = 0$ with $i \neq j$ and $\forall q_i, q_j \in Q$.

Given that each spatial data point comprises a collection of wind-speed time-indexed records, denoted as X_t, which are assumed to be distributed according to a parametrized distribution $F(x|\,\mathrm{WP})$. If the distribution function for the occurrence of weather pattern WP_i is given by $G(\mathrm{WP})$, the distribution function of X_t can be expressed as: $F_{X_t}(x) = \sum_{j=1}^{K} F(x|\,\mathrm{WP}_j)\, G(\mathrm{WP}_j)$. Therefore, the random variable X_t is marginalized over the latent distribution $G(\mathrm{WP})$ to obtain the compound distribution $F_{X_t}(x)$. The reported results primarily focused on characterizing the marginal distribution of daily wind speed, as our interests are twofold: first, to identify the most representative marginal distribution for the wind field of continental Mexico; and second, to ascertain whether there are significant changes in the wind speed distribution in response to synoptic transformations of weather patterns. Further research will be conducted to establish a probabilistic framework for forecasting the wind field, which will necessitate a comprehensive understanding of the properties of the latent distribution $G(W)$ to be used within a state-space representation.

Following the "index-flood" procedure [39], each spatial data point belonging to the region of continental Mexico, hereafter referred to as a site, possesses a collection of wind-speed time-indexed records $X_{t|\,\mathrm{WP}_j}$. These records are scaled relative to their average value, i.e., $\mu_{i,j} = E[X_{t|\,\mathrm{WP}_j}]$ for $i = \{1, \ldots, N_s\}$ and $j = \{1, \ldots, N\}$. Thus, there will be a set of site-dependent scaled data that adhere to the same regional frequency distribution. In the initial instance, the SOM algorithm yields a partition Q consisting of $N = 15$ subsets, each corresponding to a distinct dominant weather pattern WP_j. Figure 6 shows the empirical relationships between the sample L-moment ratios for some records $X_{t|\,\mathrm{WP}_j}$, with $j = 1, 7, 9, 14$, belonging to the partition obtained with the SOM algorithm. The cloud of points observed in the L-moment ratio diagrams of Figure 6 reveals the extensive spatial variability in wind speed over the continental region of Mexico. The center of the cloud of points, which is denoted by a plus sign (+), indicates the regional L-moment statistics, and discordant observations are indicated in red dots. A concentric ellipse is also plotted, with its major and minor axes determined by the sample covariance matrix of the L-moment ratios.

In the context of the L-moment diagram τ_3 vs τ, a concentric ellipse was constructed to delineate potential homogeneous regions. The ellipse's minor and major axes were determined by the covariance matrix of the L-moment ratios τ_3 and τ. This visualization helps identify sites that may be considered statistically homogeneous. However, it is important to note that local atmospheric circulation systems can introduce significant biases in the L-moment statistics compared to regional statistics. Therefore, data points that deviate from the expected regional pattern may not accurately reflect the regional statistical model and should be excluded from subsequent statistical analyses. Finally, it is noteworthy that the values of the heterogeneity measure, H, computed from the non-discordant data indicate a homogeneous region, which is suitable for selecting a regional probability distribution model.

Figure 6 also illustrates the theoretical relationship between the L-moment ratios τ_3 and τ_4 for various well-established probability distribution families, including Generalized Logistic (GLO), Generalized Extreme Value (GEV), Generalized Pareto (GPD), Exponential (Exp.), Gumbel, and Weibull. Additionally, it presents empirical estimates of these L-moment ratios for the four groups of wind speed data identified by the KMC algorithm, at each site within continental Mexico. As expected, the three-parameter Weibull distribution family exhibits the most proximity to the center of the cloud of points in the L-moment diagram. Consequently, the Weibull distribution appears to be an appropriate distribution for the regional representation of the statistical structure of wind speed over the continental region of Mexico. Nevertheless, the results of the goodness-of-fit statistical tests indicate that only the dataset associated to the weather type WP_{13} exhibits the most favorable match to the Weibull distribution for a significance level $\alpha = 0.10$, as shown in Table 1. Conversely, the four-parameter Kappa distribution, also used to fit the 15 groups of wind-speed datasets, exhibits a superior alignment with the statistical description of the data at the same significance level.

Based on previous results, the Kappa distribution is deemed the most suitable choice for describing wind speed over the continental region of Mexico. In addition, the statistical comparison between the regional and site-fitted models was conducted to assess differences between the two models. It is important to note that the site statistics were estimated at the locations of the wind farms in the current Mexican WPS to identify differences relative to the regional model. Figure 6 shows the regional growth curves of Weibull and Kappa distributions. As shown in Figure 6, there exists an overall preservation of the statistical structure observed in the site and regional growth curves. Nevertheless, significant

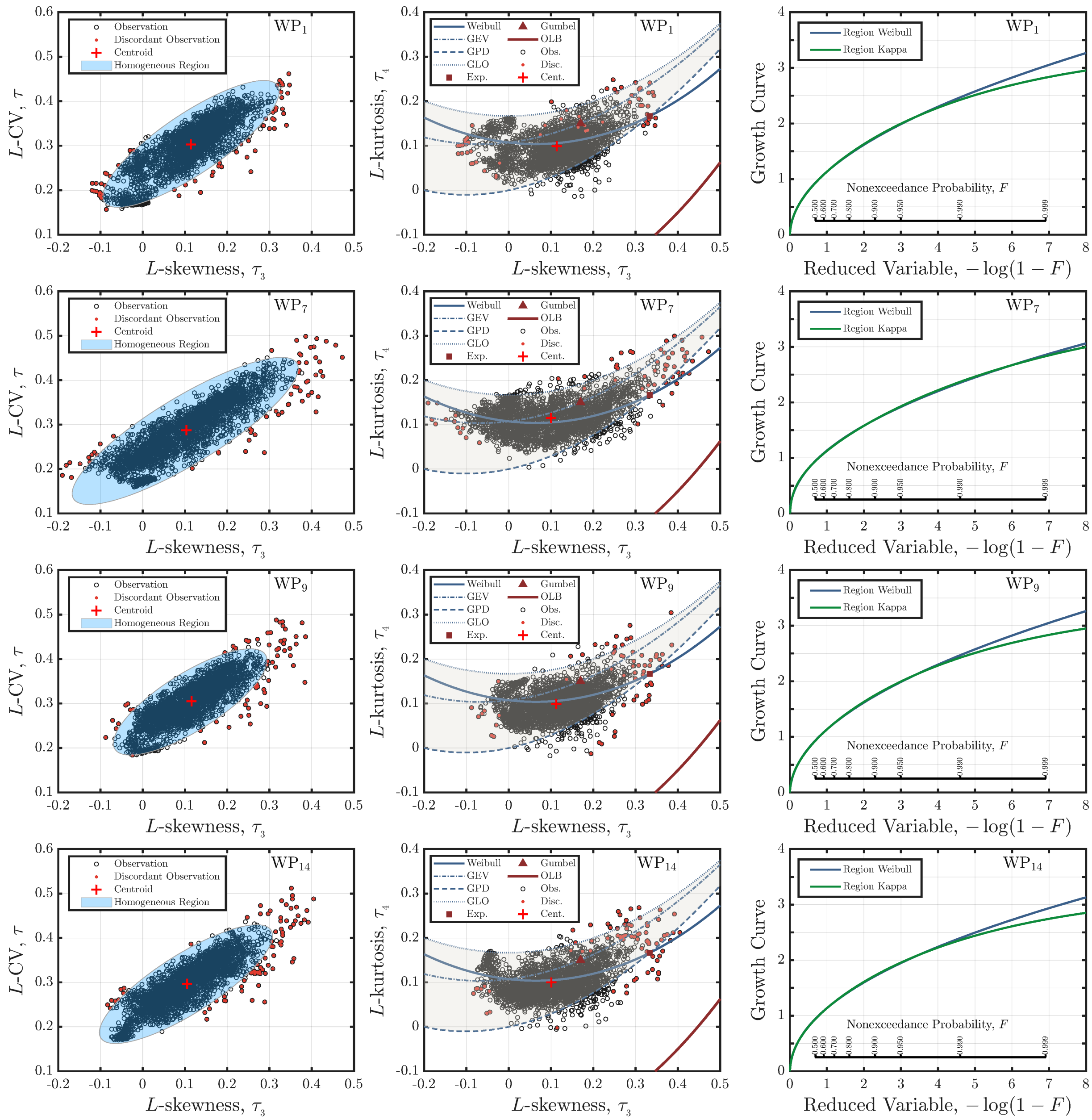

Figure 6: L-moment ratio diagrams and growth curves wind speed data for a subset of the SOM partition.

deviations can be identified at the tails of the distributions, but the best representation of the extreme values is obtained with the Weibull distribution. Complementarily, Figure 7 shows the distribution of relative bias between the regional and site statistics (i.e., $(Q_{reg} - Q_{loc})/Q_{loc}$). These statistics shown in Figure 7 are: the first quartile Q_{25}, the median Q_{50}, the third quartile Q_{75}, the 90th percentile Q_{90} and the 95th quantile Q_{95}.

As observed, either the Weibull or Kappa regional distributions yield statistics that exceed the site estimates, suggesting that our regional model is subject to greater uncertainty when estimating quantiles at the extremes of the distribution. Conversely, moderate variability is observed in the statistics that specify central tendency. Since the central tendency statistics indicate lower variability, the regional statistical model performs more effectively at describing the central body of the probability distribution. It is highligted that the design and regular operation of most wind farms depend on the central-tendency statistics (e.g., most probable wind speed), therefore, the regional model remains suitable for the statistical description of wind speed in the continental region of Mexico. Nevertheless, caution should be exercised when estimating extremes.

Table 1: Statistical summary of the L-moment ratios values and fitted distribution parameters for the SOM partition of wind speed data.

	L-moment					Weibull Distribution						Kappa Distribution						
WP	μ	τ^{R}	τ_3^{R}	τ_4^{R}	H^a	k	A	B	τ_4^{D}	Z^{D}	p[b]	ξ	α	k	h	τ_4^{D}	Z^{D}	p
1	3.026	0.303	0.114	0.100	-1.843	2.003	1.170	-0.037	0.105	7.445	<0.001	0.651	0.618	0.224	0.343	0.099	0.005	0.996
2	3.231	0.301	0.110	0.096	-1.901	2.034	1.177	-0.043	0.105	11.781	<0.001	0.642	0.634	0.244	0.371	0.095	0.008	0.994
3	3.073	0.302	0.113	0.098	-1.961	2.022	1.174	-0.041	0.105	9.770	<0.001	0.647	0.626	0.235	0.357	0.097	-0.022	0.983
4	2.869	0.290	0.094	0.100	-1.824	2.204	1.210	-0.072	0.104	6.954	<0.001	0.697	0.578	0.240	0.277	0.098	-0.008	0.994
5	2.853	0.296	0.117	0.116	-1.683	1.993	1.137	-0.008	0.105	-9.974	<0.001	0.714	0.530	0.157	0.191	0.114	-0.001	0.999
6	2.840	0.307	0.121	0.103	-1.881	1.958	1.158	-0.027	0.106	4.472	<0.001	0.650	0.613	0.208	0.334	0.102	0.005	0.996
7	3.043	0.287	0.103	0.117	-1.710	2.118	1.157	-0.025	0.104	-12.647	<0.001	0.747	0.499	0.160	0.131	0.115	0.018	0.986
8	2.948	0.295	0.112	0.112	-1.821	2.045	1.152	-0.021	0.105	-5.775	<0.001	0.711	0.541	0.178	0.214	0.110	0.015	0.988
9	2.768	0.305	0.115	0.100	-2.092	2.012	1.175	-0.041	0.105	7.224	<0.001	0.652	0.617	0.224	0.339	0.099	0.018	0.985
10	3.016	0.290	0.102	0.109	-1.861	2.122	1.171	-0.037	0.104	-4.044	<0.001	0.720	0.536	0.192	0.206	0.108	-0.003	0.998
11	2.907	0.295	0.109	0.109	-2.085	2.071	1.164	-0.031	0.105	-3.840	<0.001	0.709	0.547	0.188	0.223	0.108	0.014	0.989
12	2.771	0.304	0.113	0.098	-2.038	2.026	1.181	-0.047	0.105	9.092	<0.001	0.648	0.625	0.233	0.350	0.097	0.019	0.985
13	2.918	0.295	0.105	0.105	-1.910	2.104	1.179	-0.044	0.104	0.987	0.324	0.698	0.565	0.209	0.255	0.104	-0.009	0.993
14	2.839	0.297	0.105	0.102	-1.833	2.112	1.190	-0.054	0.104	5.423	<0.001	0.683	0.587	0.226	0.291	0.100	0.006	0.995
15	2.906	0.305	0.119	0.104	-1.846	1.977	1.160	-0.028	0.106	3.520	<0.001	0.659	0.603	0.206	0.318	0.103	-0.012	0.990

[a]This is the heterogeneity index, which is employed to assess the homogeneity degree of the study region in conjunction with the data sub-sampling.
[b]This represents the p-value.

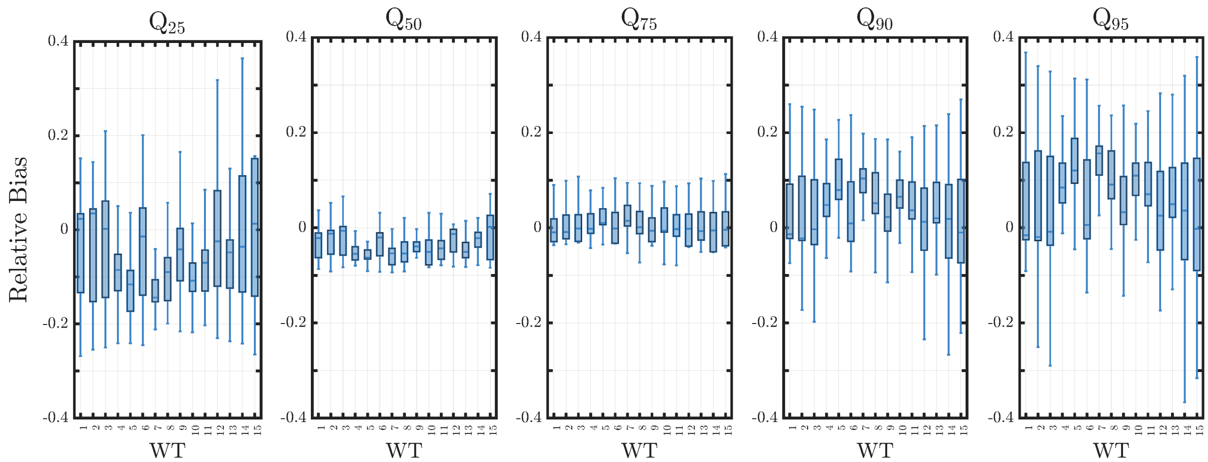

(a) Weibull Probability Distribution.

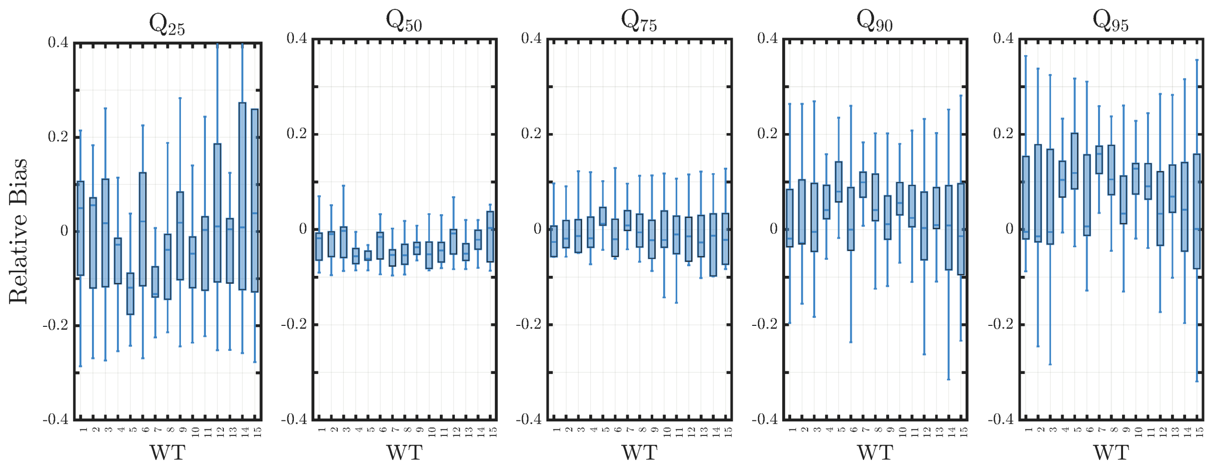

(b) Kappa Probability Distribution

Figure 7: Relative biases of quantile values of wind speed between the site and the regional statistical models. Fifteen groups of quantile values were considered for this plot, as they represent the fifteen weather patterns obtained by the SOM algorithm. Site statistics were computed at the locations of the wind farms in the current Mexican WPS. The statistical models that were considered for this analysis are: 1) the three-parameter Weibull probability distribution and 2) the four-parameter Kappa probability distribution. From left to right, each panel illustrates the bias for the first quartile (Q_{25}), the median (Q_{50}), the third quartile (Q_{75}), the 90th percentile (Q_{90}), and the 95th percentile (Q_{95}).

Thus far, it is noteworthy that the four-parameter Kappa probability distribution accurately describes the wind-speed datasets derived from partitions generated by the KMC and SOM algorithms. Furthermore, there are no relative biases exceeding 15% between regional and site statistics within the central region of the Kappa probability distribution. Therefore, the Kappa distribution emerges as the superior model for regional wind speed description. Now, it is crucial to emphasize that there are no pivotal transformations in the distribution of wind speed during the transitions between weather patterns. The test conducted using the KL divergence measure, $D_{\mathrm{KL}}(F_i||F_j)$, indicates that there are no statistically significant changes in distribution with an average false rejection rate of approximately 4.8% across the majority of transitions between weather patterns. However, the weather pattern WP_5 identified within the SOM partition exhibits the most pronounced disparity in distribution compared to the other distributions, as evidenced in Table 2. These findings may suggest that the wind-speed data used to estimate the distributions were sampled incorrectly, resulting in a covariate shift in the resulting distributions. Furthermore, recalling the total probability theorem, the estimation of the probability distribution function of wind speed can be generalized by $\Pr\{X_j \leq x\} = \sum \Pr\{X_j \leq x|\,\mathrm{WP}_i\}\ \Pr\{\mathrm{WP}_i\}$; where $\Pr\{\mathrm{WP}_i\}$ is the probability of occurrence of the weather pattern WP_i and $\Pr\{X_j \leq x|\,\mathrm{WP}_i\}$ is the conditional probability of the wind speed given the occurrence of the weather pattern WP_i. Consequently, if a stationary distribution for the occurrence of weather patterns, π, exists, one would anticipate that the conditional probability of the wind speed should remain time invariant to maintain a stationary distribution of the wind speed. Based on the aforementioned, the probability distributions reported in Table 1 do not indicate structural breaks, as these distributions appear to be constrained to the stationary condition of the wind-speed field for the continental region of Mexico.

Based on the aforementioned results, the regional analysis aims to improve the characterization of the dependencies between LSWP and the wind-speed field. Furthermore, this analysis assesses the suitability of the Weibull distribution for describing the marginal probability distribution of the wind-speed field. In this context, our findings suggest that the Weibull distribution may not be the most appropriate model for the statistical characterization of local wind speed records at the regional scale. Instead, the four-parameter Kappa distribution appears to provide a more accurate representation of the overall statistical structure of these records. Moreover, the Kappa distribution is particularly well-suited to characterizing measures of central tendency, which are commonly used in the design and evaluation of wind power systems. A crucial aspect to emphasize in the context of LSWP classification and its inherent probabilistic model of wind speed is the absence of significant structural variations in the distributions. This finding primarily suggests that regional wind speed can be characterized as a stationary process with moderate dependence on weather patterns.

3.3 Potential Wind Energy Assessment

Up to this point, the prior analysis has enabled us to identify a suitable statistical representation of the regional behavior of wind speed in relation to the occurrence of fifteen dominant weather patterns prevalent over Mexico. Subsequently, the results present an assessment of the impact of weather patterns on wind energy production across seven sub-regions of continental Mexico, which encompass the majority of wind farms in the Mexican WPS.

First of all, Figures 8 and 9 present two sets of maps that illustrate the potential wind energy resources available for the continental region of Mexico in terms of the values for the wind power density and maximum energy production. As depicted in Figure 8, the highest wind power density values are situated in the Mexican states of Tamaulipas and Nuevo León (northeast), Baja California (northwest), Zacatecas and San Luis Potosí (central), Oaxaca (south), and the Yucatán Peninsula (southeast). In essence, the majority of the WPS has been developed in the aforementioned sub-regions, which align with the most suitable locations for establishing wind farm construction. However, synoptic atmospheric variability modulates the wind field over time, resulting in spatio-temporal variations in wind power density. For instance, Figure 8 illustrates that the occurrence of weather pattern WP_2 increases wind power density in the majority of the current location of the WPS wind farms, while conversely, the occurrence of weather pattern WP_{11} leads to a significant reduction in wind power density, resulting in a low wind energy production that imply a higher utilization of alternative energy sources.

Similarly, the spatial variability of the maximum energy density is comparable to that observed for the wind power density. However, since the annual maximum energy density is determined by the average time of annual occurrence of a specific weather pattern, Figure 9 demonstrates that there is an uneven contribution of wind energy throughout the year, which is mainly influenced by the frequency of occurrence of weather patterns. As shown in Table 3, the highest energy contribution is observed when the weather patterns WP_1, WP_2, and WP_3 occur. These patterns are expected to occur more frequently each month, with higher frequency during the winter and mid-spring seasons. Conversely, the lowest energy contribution is observed when the weather patterns WP_5, WP_{14}, and WP_{15} occur. However, these patterns are less frequent throughout the year.

Table 3 presents the results of wind power density and maximum energy density in some important Mexican sub-regions, elucidating the impact of synoptic atmospheric variability on the potential wind energy production within the Mexican territory. Furthermore, the results underscore the imperative of enhanced operational control measures to optimize energy production while minimizing disturbances to the stability of the current MES. Oaxaca is considered the most valuable region for energy production in Mexico, with an expected energy yield of approximately 11,000 kWh/m^2. However, this region exhibits the highest intra-annual variability, resulting in significant fluctuations in energy yield. Furthermore, Oaxaca's region exhibits contrasting wind power density compared to other Mexican regions. As illustrated in Figure 9, weather patterns WP_1, WP_2, and WP_3 predominantly enhance wind power density, while patterns WP_7 and WP_{11} define scenarios where wind power density is reduced. Nevertheless, as indicated in Table 3, the aforementioned weather patterns exert a dissimilar effect on Oaxaca's region.

The occurrence of the most frequent weather patterns, i.e., WP_1, WP_2, and WP_3, points out a reduction in energy production at the most critical region for energy extraction. Our findings emphasize that variability in weather patterns leads to fluctuations in load service, requiring the reservation of capacity (or spinning reserve) to compensate for wind generation variability and maintain system frequency stability. However, scheduling spinning reserve for higher wind power penetration in the electrical system increases operating costs and exacerbates the deterioration of wind turbine mechanical components. Although our current scope does not include developing a probabilistic framework to optimize

Table 2: Rejection rates of the null hypothesis, which ascertains that both distributions belong to the same distribution based on the KL divergence measure. The rejection rates were computed from $1,000$ random sample sets. These sample sets were generated using the parameters of the Kappa probability distributions presented in Table 1.

	WP_1	WP_2	WP_3	WP_4	WP_5	WP_6	WP_7	WP_8	WP_9	WP_{10}	WP_{11}	WP_{12}	WP_{13}	WP_{14}	WP_{15}
WP_1	-	0.020	0.007	0.024	0.149	0.009	0.018	0.010	0.010	0.005	0.001	0.030	0.004	0.023	0.044
WP_2	-	-	0.027	0.042	0.150	0.034	0.045	0.030	0.041	0.027	0.033	0.042	0.040	0.055	0.068
WP_3	-	-	-	0.016	0.129	0.004	0.011	0.007	0.015	0.010	0.008	0.026	0.004	0.030	0.045
WP_4	-	-	-	-	0.151	0.018	0.016	0.009	0.029	0.011	0.009	0.043	0.008	0.037	0.075
WP_5	-	-	-	-	-	0.147	0.177	0.105	0.139	0.166	0.131	0.191	0.136	0.193	0.210
WP_6	-	-	-	-	-	-	0.033	0.007	0.017	0.010	0.005	0.022	0.008	0.045	0.055
WP_7	-	-	-	-	-	-	-	<0.001	0.027	<0.001	<0.001	0.048	<0.001	0.058	0.117
WP_8	-	-	-	-	-	-	-	-	0.017	<0.001	0.001	0.044	<0.001	0.028	0.057
WP_9	-	-	-	-	-	-	-	-	-	0.015	0.022	0.039	0.016	0.037	0.057
WP_{10}	-	-	-	-	-	-	-	-	-	-	0.002	0.029	<0.001	0.046	0.072
WP_{11}	-	-	-	-	-	-	-	-	-	-	-	0.031	<0.001	0.033	0.065
WP_{12}	-	-	-	-	-	-	-	-	-	-	-	-	0.035	0.055	0.059
WP_{13}	-	-	-	-	-	-	-	-	-	-	-	-	-	0.023	0.070
WP_{14}	-	-	-	-	-	-	-	-	-	-	-	-	-	-	0.070
WP_{15}	-	-	-	-	-	-	-	-	-	-	-	-	-	-	-

Table 3: Comparative analysis of wind power density and percentage maximum energy production in relation to the LSWP occurrence.

	Wind Power Density[1], $P_d(u\|\mathrm{WP}_j)$ [W m^{-2}]															
	WP_1	WP_2	WP_3	WP_4	WP_5	WP_6	WP_7	WP_8	WP_9	WP_{10}	WP_{11}	WP_{12}	WP_{13}	WP_{14}	WP_{15}	Avg.
Baja California	107	123	88	69	69	71	56	48	59	50	45	72	63	68	99	73
Coahuila	105	114	103	116	115	91	122	104	89	119	102	96	127	124	123	110
Nuevo León	173	210	187	158	196	164	152	127	125	133	110	129	141	140	178	155
Oaxaca	240	189	221	430	404	313	692	734	422	622	648	319	450	309	191	412
Tamaulipas	193	243	209	154	193	173	145	126	128	128	113	132	137	135	184	160
Yucatán	132	145	127	111	106	102	109	121	98	121	114	93	123	105	90	113
Zacatecas	77	91	84	71	72	66	95	84	63	91	83	64	81	68	69	77

	Maximum Energy Density, $W_{\max}$ [kWh m^{-2}]															
	WP_1	WP_2	WP_3	WP_4	WP_5	WP_6	WP_7	WP_8	WP_9	WP_{10}	WP_{11}	WP_{12}	WP_{13}	WP_{14}	WP_{15}	Total
Baja California	15%	16%	18%	4%	1%	8%	3%	5%	5%	4%	3%	5%	9%	2%	3%	2,177
Coahuila	11%	10%	15%	4%	1%	7%	4%	7%	5%	7%	6%	5%	13%	3%	3%	3,079
Nuevo León	12%	13%	18%	4%	1%	9%	3%	6%	5%	5%	4%	5%	10%	2%	3%	4,483
Oaxaca	7%	5%	9%	4%	1%	7%	6%	15%	7%	10%	10%	5%	13%	2%	1%	11,074
Tamaulipas	13%	14%	19%	4%	1%	9%	3%	6%	5%	5%	4%	4%	9%	2%	3%	4,738
Yucatán	12%	12%	16%	4%	1%	7%	3%	8%	5%	6%	6%	4%	11%	2%	2%	3,383
Zacatecas	11%	11%	16%	4%	1%	7%	4%	8%	5%	7%	6%	5%	11%	2%	2%	2,256

Wind power density values, presented in red and blue font colors, refer to positive and negative fluctuations, respectively, in comparison to the sub-regional average values.

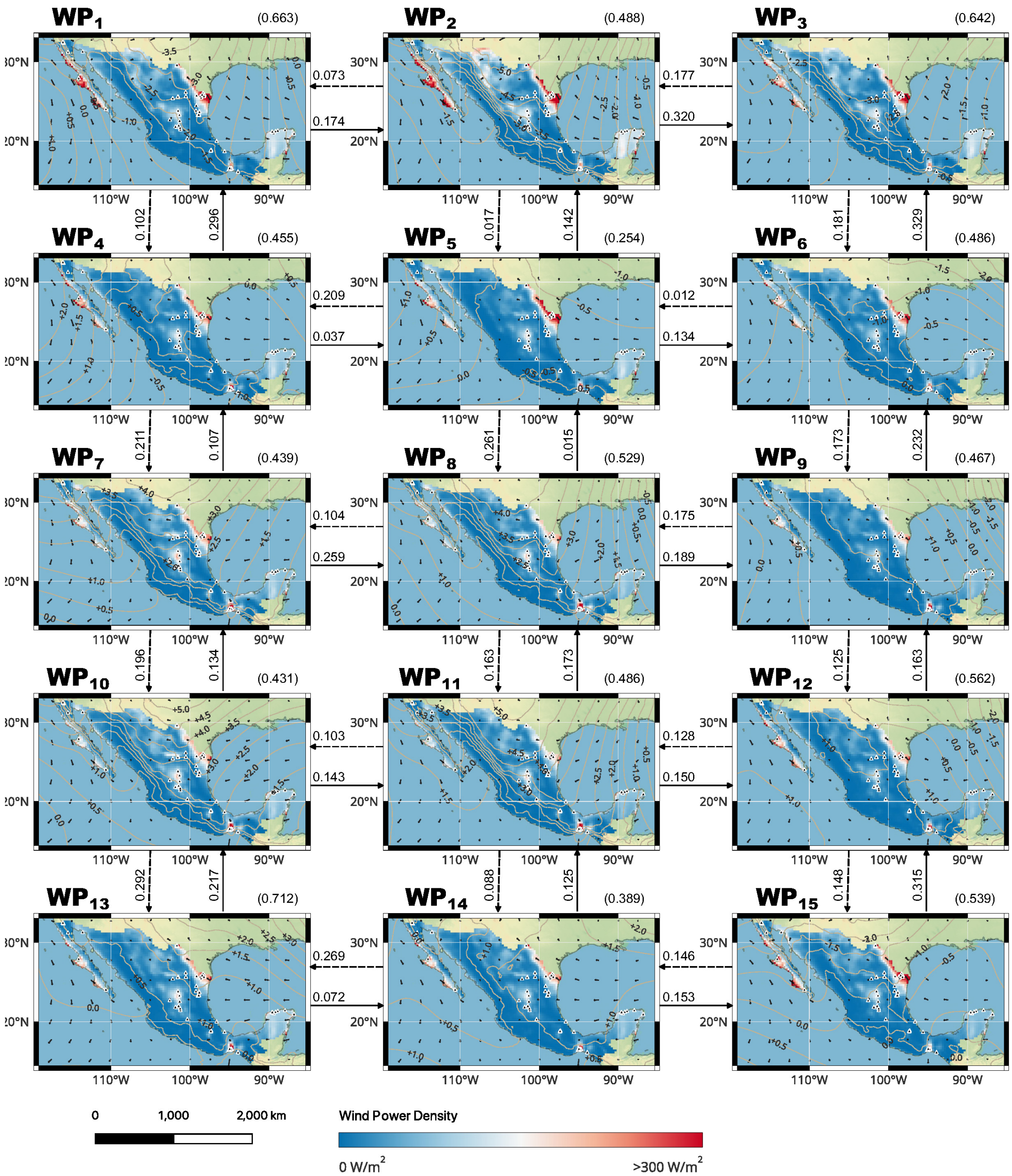

Figure 8: Map of potential wind power density across the continental region of Mexico, based on the occurrence of the LSWP that were detected by the SOM algorithm. All the plots illustrate wind velocity vectors and the isolines of pressure anomaly (dashed lines).

the operation of the Mexican electrical system in response to changes in weather patterns, we recommend conducting such a study in future projects. This study should also include an uncertainty assessment that enables operators to develop more effective contingency strategies.

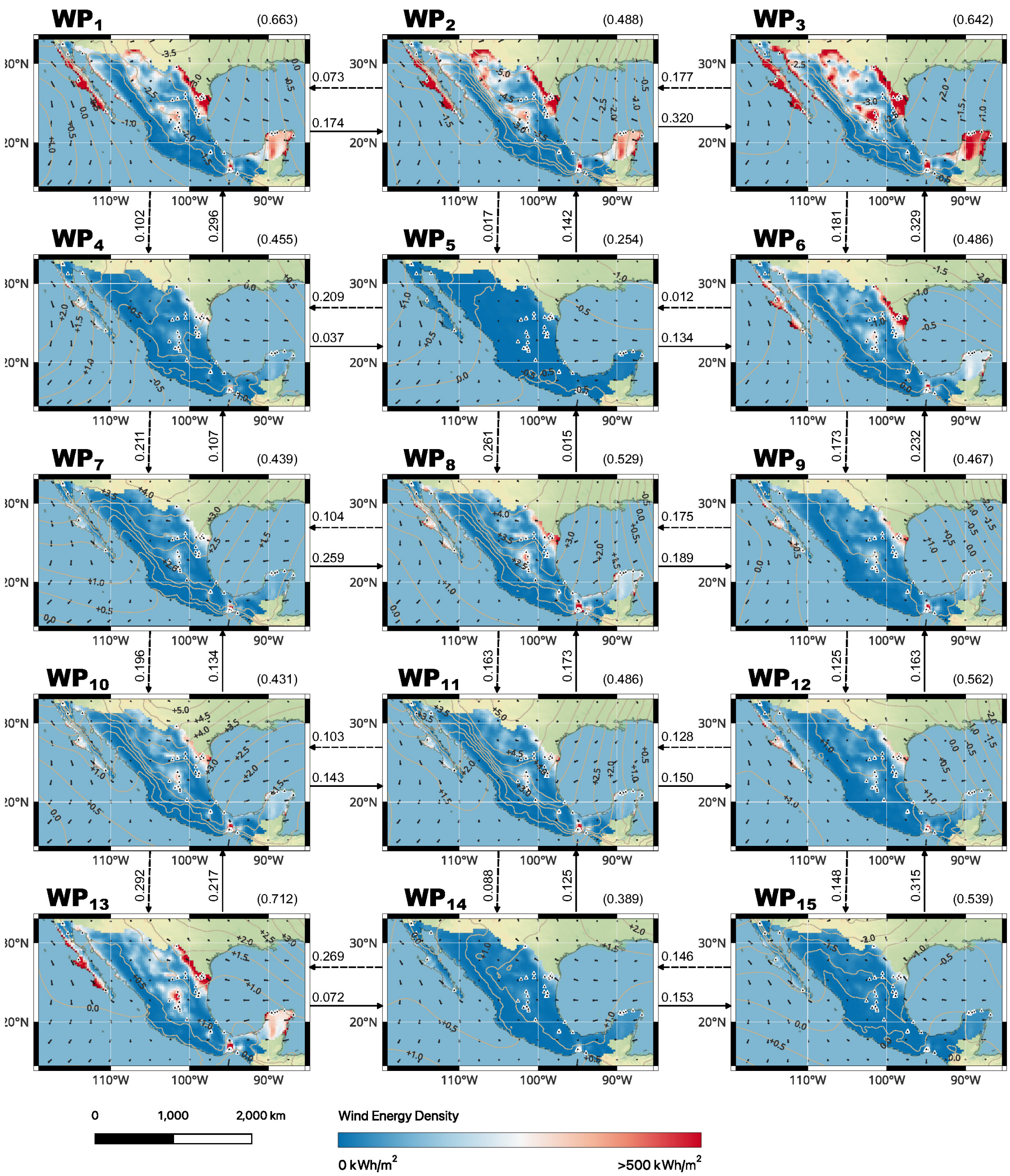

Figure 9: Map of maximum wind energy production across the continental region of Mexico, based on the occurrence of the LSWP that were detected by the SOM algorithm. All the plots illustrate wind velocity vectors and the isolines of pressure anomaly (dashed lines).

4 Conclusions

A regional wind-speed probabilistic model, along with a weather-pattern classification analysis, was employed to assess the influence of large-scale weather patterns on the regional wind-speed field, estimate potential wind energy across the continental region of Mexico, and establish a connection between this potential and fluctuations in large-scale weather patterns. Evidently, there is a diversity of wind-power classes across Mexico that effectively reflects substantial spatial variability in the wind-speed field. Furthermore, there are noteworthy variations in these wind-power classes in relation to the occurrence of weather patterns. Oaxaca's region is recognized as the most valuable region for energy generation. However, this region is susceptible to variability in weather patterns, resulting in the largest and most pronounced fluctuations in potential energy compared with other Mexican regions. This suggests that the stability of the Mexican electrical system can be significantly influenced by synoptic atmospheric variability. Consequently, the grid system's response should be integrated with other energy sources to ensure a consistent energy supply nationwide while minimizing operational costs.

Declarations

Data availability

The ERA5 Daily Mean Sea Level Pressure Anomalies and 100m-Wind Velocity data files, which serve as the foundation for this research, are available for access in the Harvard Dataverse online repository [63]. These files can be accessed via the following URL address: `https://doi.org/10.7910/DVN/L8AGSP`.

Additional data regarding the research findings can be obtained upon request.

Codes availability

The codes or MATLAB scripts that were employed in the research process can be made available upon request.

Funding

This research was funded by the Federal Electricity Commission (CFE) under the project Implementation of the Meteorological Forecast System for the Estimation of Energy Production in Mexican Wind and Photovoltaic Farms, Ref. CFE–ICL–2021.

Author contribution

The contributions from the authors Victor M. Peñaranda-Vélez and Carlos A. Ochoa-Moya are: Conceptualization of this study, Methodology, Formal analysis, Software, Data curation, and Writing - Original draft. The contributions by Arturo I. Quintanar are: Conceptualization of this study, Methodology, Formal analysis and Review - Original draft.

References

[1] SENER. Programa de desarrollo del sistema eléctrico nacional 2024-2038. Technical report, Secretaría de Energía de México, 2024.

[2] Tsang-Jung Chang and Yi-Long Tu. Evaluation of monthly capacity factor of wecs using chronological and probabilistic wind speed data: A case study of taiwan. *Renewable Energy*, 32:1999–2010, 10 2007.

[3] AMDEE. Informe Anual AMDEE 2025. Technical report, Asociación Mexicana de Energía Eólica, 2025.

[4] SEGOB. La energía eólica en méxico: una perspectiva social sobre el valor de la tierra. Technical report, Secretaría de Gobernación, 2012.

[5] Miguel Cortez and Jun Matsumoto. Cambios intraestacionales en la circulación regional sobre méxico. *Investigaciones geográficas*, pages 30–44, 9 2001.

[6] Gabriela Colorado-Ruiz and Tereza Cavazos. Identifying patterns of summer precipitation and extremes in eastern mexico with self-organizing maps: large scale and regional drivers. *Climate Dynamics*, 63:220, 5 2025.

[7] Carlos A Ochoa-Moya, Yoel A Cala-Pérez, Yanet Díaz-Esteban, Christopher L. Castro, Paulina Ordoñez-Peréz, and Arturo I Quintanar. Climatological large-scale circulation patterns over the middle americas region. *Atmosphere*, 11:745, 7 2020.

[8] Ernesto Jáuregui Ostos. Variaciones de largo periodo de los tipos de tiempo de superficie en méxico. *Investigaciones Geográficas*, 1, 1 1971.

[9] Simon Richard Thomas, Oscar Martínez-Alvarado, Daniel Drew, and Hannah Bloomfield. Drivers of extreme wind events in mexico for windpower applications. *International Journal of Climatology*, 41, 1 2021.

[10] Sebastian Springer, Alessandro Laio, Vera Melinda Galfi, and Valerio Lucarini. Unsupervised detection of large-scale weather patterns in the northern hemisphere via markov state modelling: from blockings to teleconnections. *npj Climate and Atmospheric Science*, 7:105, 5 2024.

[11] Andrew W Robertson and Michael Ghil. Large-scale weather regimes and local climate over the western united states. *Journal of Climate*, 12:1796–1813, 6 1999.

[12] Michael Ghil and Andrew W Robertson. "waves" vs. "particles" in the atmosphere's phase space: A pathway to long-range forecasting? *Proceedings of the National Academy of Sciences*, 99:2493–2500, 2 2002.

[13] Christian M Grams, Remo Beerli, Stefan Pfenninger, Iain Staffell, and Heini Wernli. Balancing europe's wind-power output through spatial deployment informed by weather regimes. *Nature Climate Change*, 7:557–562, 8 2017.

[14] Karla Pereyra-Castro, Ernesto Caetano, Oscar Martínez-Alvarado, and Ana L. Quintanilla-Montoya. Wind and wind power ramp variability over northern mexico. *Atmosphere*, 11(12):1281, 2020.

[15] Laurie Agel, Mathew Barlow, Steven B. Feldstein, and William J. Gutowski. Identification of large-scale meteorological patterns associated with extreme precipitation in the us northeast. *Climate Dynamics*, 50:1819–1839, 3 2018.

[16] Fernando Arizmendi, Romina Trinchin, and Marcelo Barreiro. Weather regimes in subtropical south america and their impacts over uruguay. *International Journal of Climatology*, 42:9253–9270, 12 2022.

[17] Boris A. Babanov and Vladimir A. Semenov. Weather regimes in northern eurasia: Statistics, predictability and associated weather anomalies. *Atmosphere*, 15:1392, 11 2024.

[18] Alessandro Baldo and Robin Locatelli. A probabilistic view on modelling weather regimes. *International Journal of Climatology*, 43:1710–1730, 3 2023.

[19] Mathew Barlow, William J. Gutowski, John R. Gyakum, Richard W. Katz, Young-Kwon Lim, Russ S. Schumacher, Michael F. Wehner, Laurie Agel, Michael Bosilovich, Allison Collow, Alexander Gershunov, Richard Grotjahn, Ruby Leung, Shawn Milrad, and Seung-Ki Min. North american extreme precipitation events and related large-scale meteorological patterns: a review of statistical methods, dynamics, modeling, and trends. *Climate Dynamics*, 53:6835–6875, 12 2019.

[20] Joseph Barsugli, Sang-Ik Shin, and Prashant D. Sardeshmukh. Tropical climate regimes and global climate sensitivity in a simple setting. *Journal of the Atmospheric Sciences*, 62:1226–1240, 4 2005.

[21] EN Cassano, JM Glisan, JJ Cassano, WJ Gutowski, and MW Seefeldt. Self-organizing map analysis of widespread temperature extremes in alaska and canada. *Climate Research*, 62:199–218, 2 2015.

[22] Swinda K.J. Falkena, Jana de Wiljes, Antje Weisheimer, and Theodore G. Shepherd. Revisiting the identification of wintertime atmospheric circulation regimes in the euro-atlantic sector. *Quarterly Journal of the Royal Meteorological Society*, 146:2801–2814, 7 2020.

[23] F. Garavaglia, J. Gailhard, E. Paquet, M. Lang, R. Garçon, and P. Bernardara. Introducing a rainfall compound distribution model based on weather patterns sub-sampling. *Hydrology and Earth System Sciences*, 14:951–964, 6 2010.

[24] Paul-Antoine Michelangeli, Robert Vautard, and Bernard Legras. Weather regimes: Recurrence and quasi stationarity. *Journal of Atmospheric Sciences*, 52(8):1237 – 1256, 1995.

[25] Robert Neal, David Fereday, Ric Crocker, and Ruth E Comer. A flexible approach to defining weather patterns and their application in weather forecasting over europe. *Meteorological Applications*, 23:389–400, 7 2016.

[26] Kyle Shackelford, Charlotte A. DeMott, Peter Jan van Leeuwen, and Elizabeth A. Barnes. A regimes-based approach to identifying seasonal state-dependent prediction skill. *Journal of Geophysical Research: Atmospheres*, 130, 4 2025.

[27] Daniel F. Rex. Blocking action in the middle troposphere and its effect upon regional climate. *Tellus*, 2:196–211, 8 1950.

[28] Ebrahim Nabizadeh, Pedram Hassanzadeh, Da Yang, and Elizabeth A Barnes. Size of the atmospheric blocking events: Scaling law and response to climate change. *Geophysical Research Letters*, 46:13488–13499, 11 2019.

[29] Daniel Steinfeld, Michael Sprenger, Urs Beyerle, and Stephan Pfahl. Response of moist and dry processes in atmospheric blocking to climate change. *Environmental Research Letters*, 17:084020, 8 2022.

[30] Tania Buehler, Christoph C Raible, and Thomas F Stocker. The relationship of winter season north atlantic blocking frequencies to extreme cold or dry spells in the era-40. *Tellus A*, 63:212–222, 3 2011.

[31] Elena Xoplaki, Ricardo M Trigo, Ricardo García-Herrera, David Barriopedro, Fabio D'andrea, Erich M Fischer, Luis Gimeno, Celia Gouveia, Emiliano Hernández, Franz G Kuglitsch, Annarita Mariotti, Raquel Nieto, Joaquim G Pinto, D Pozo-Vázquez, Hadas Saaroni, Andrea Toreti, Isabel F Trigo, Sergio M Vicente-Serrano, Pascal Yiou, and Baruch Ziv. Large-scale atmospheric circulation driving extreme climate events in the mediterranean and

related impacts. In Piero Lionello, editor, *The Climate of the Mediterranean Region*, chapter 6, pages 347–417. Elsevier, Italy, 2012.

[32] Tim Woollings, David Barriopedro, John Methven, Seok-Woo Son, Olivia Martius, Ben Harvey, Jana Sillmann, Anthony R. Lupo, and Sonia Seneviratne. Blocking and its response to climate change. *Current Climate Change Reports*, 4:287–300, 9 2018.

[33] Melanie Bieli, Stephan Pfahl, and Heini Wernli. A lagrangian investigation of hot and cold temperature extremes in europe. *Quarterly Journal of the Royal Meteorological Society*, 141:98–108, 1 2015.

[34] Peter B. Gibson, Sarah E. Perkins-Kirkpatrick, Petteri Uotila, Acacia S. Pepler, and Lisa V. Alexander. On the use of self-organizing maps for studying climate extremes. *Journal of Geophysical Research: Atmospheres*, 122(7):3891–3903, 2017.

[35] Gary L. Johnson. *Wind energy systems*. Prentice-Hall, Manhattan, 1985.

[36] G. Gualtieri. Analysing the uncertainties of reanalysis data used for wind resource assessment: A critical review. *Renewable and Sustainable Energy Reviews*, 167:112741, 2022.

[37] C.F. Morales-Ruvalcaba, O. Rodríguez-Hernández, O. Martínez-Alvarado, D.R. Drew, and E. Ramos. Estimating wind speed and capacity factors in mexico using reanalysis data. *Energy for Sustainable Development*, 58:158–166, 10 2020.

[38] Rajat Kanti Samal. Assessment of wind energy potential using reanalysis data: A comparison with mast measurements. *Journal of Cleaner Production*, 313:127933, 2021.

[39] J. R. M. Hosking and J. R. Wallis. Some statistics useful in regional frequency analysis. *Water Resources Research*, 29:271–281, 2 1993.

[40] J. R. M. Hosking and James R. Wallis. *Regional Frequency Analysis*. Cambridge University Press, New York, 1997.

[41] Hans Hersbach, Bill Bell, Paul Berrisford, Shoji Hirahara, Andras Horanyi, Joaquin Muñoz Sabater, Julien Nicolas, Carole Peubey, Raluca Radu, Dinand Schepers, Adrian Simmons, Cornel Soci, Saleh Abdalla, Xavier Abellan, Gianpaolo Balsamo, Peter Bechtold, Gionata Biavati, Jean Bidlot, Massimo Bonavita, Giovanna De Chiara, Per Dahlgren, Dick Dee, Michail Diamantakis, Rossana Dragani, Johannes Flemming, Richard Forbes, Manuel Fuentes, Alan Geer, Leo Haimberger, Sean Healy, Robin J. Hogan, Elias Holm, Marta Janiskova, Sarah Keeley, Patrick Laloyaux, Philippe Lopez, Cristina Lupu, Gabor Radnoti, Patricia de Rosnay, Iryna Rozum, Freja Vamborg, Sebastien Villaume, and Jean-Noel Thepaut. The era5 global reanalysis. *Quarterly Journal of the Royal Meteorological Society*, 146(730):1999–2049, 2020.

[42] Open Infrastructure Map. Mexico: Power plants. Accessed: 2025-10-13 at `https://openinframap.org/stats/area/Mexico/plants`.

[43] The Wind Power. Lista de parques eólicos. Accessed: 2025-10-13 at `https://www.thewindpower.net/windfarms_list_es.php`.

[44] Emily E. Riddle, Marshall B. Stoner, Nathaniel C. Johnson, Michelle L. L'Heureux, Dan C. Collins, and Steven B. Feldstein. The impact of the mjo on clusters of wintertime circulation anomalies over the north american region. *Climate Dynamics*, 40:1749–1766, 4 2013.

[45] Steven B. Feldstein and Sukyoung Lee. Intraseasonal and interdecadal jet shifts in the northern hemisphere: The role of warm pool tropical convection and sea ice. *Journal of Climate*, 27:6497–6518, 9 2014.

[46] Ningbo Jiang, Kehui Luo, Paul J. Beggs, Kevin Cheung, and Yvonne Scorgie. Insights into the implementation of synoptic weather-type classification using self-organizing maps: an australian case study. *International Journal of Climatology*, 35(12):3471–3485, 2015.

[47] Teuvo Kohonen. Essentials of the self-organizing map. *Neural Networks*, 37:52–65, 1 2013.

[48] Teuvo Kohonen. *Self-Organizing Maps*, volume 30. Springer Berlin Heidelberg, Berlin, Heidelberg, 3rd edition, 2001.

[49] Le Anh-Tu. Improving feature map quality of SOM based on adjusting the neighborhood function. In Amjad Almusaed, editor, *Sustainability in Urban Planning and Design*, chapter 5, pages 5.1–5.17. IntechOpen, London, 2020.

[50] Esa Alhoniemi, Johan Himberg, Jukka Parviainen, and Juha Vesanto. SOM Toolbox 2.0, a software library for MATLAB 5 implementing the self-organizing map algorithm, 1999.

[51] Himangshu Ranjan Ghosh. Wind speed weibull distribution and wind energy potential of chandpur, bangladesh. *Dhaka University Journal of Applied Science and Engineering*, 6:99–108, 6 2022.

[52] A. Keyhani, M. Ghasemi-Varnamkhasti, M. Khanali, and R. Abbaszadeh. An assessment of wind energy potential as a power generation source in the capital of iran, tehran. *Energy*, 35:188–201, 1 2010.

[53] Lin Lu, Hongxing Yang, and John Burnett. Investigation on wind power potential on hong kong islands—an analysis of wind power and wind turbine characteristics. *Renewable Energy*, 27(1):1–12, 2002.

[54] Abdullah Marashli, Mahmoud Alburdaini, Hani Al-Rawashdeh, and Mohammad Shalby. Statistical analysis of wind speed distribution based on five weibull methods for wind power evaluation in maan, jordan. *Journal of Energy Technologies and Policy*, 11:55–70, 10 2021.

[55] A. Mostafaeipour, A. Sedaghat, A.A. Dehghan-Niri, and V. Kalantar. Wind energy feasibility study for city of shahrbabak in iran. *Renewable and Sustainable Energy Reviews*, 15:2545–2556, 8 2011.

[56] F. Veronesi, S. Grassi, and M. Raubal. Statistical learning approach for wind resource assessment. *Renewable and Sustainable Energy Reviews*, 56:836–850, 4 2016.

[57] Piotr Wais. A review of weibull functions in wind sector. *Renewable and Sustainable Energy Reviews*, 70:1099–1107, 4 2017.

[58] Piotr Wais. Two and three-parameter weibull distribution in available wind power analysis. *Renewable Energy*, 103:15–29, 4 2017.

[59] Christopher Jung and Dirk Schindler. Wind speed distribution selection – a review of recent development and progress. *Renewable and Sustainable Energy Reviews*, 114:109290, 10 2019.

[60] Hui Ding, Michael A. Alexander, and Mingfang Ting. Revisiting the relationship between the north pacific high and upwelling winds along the west coast of north america in the present and future climate. *Journal of Climate*, 36(23):8211 – 8224, 2023.

[61] M. J. Rodwell and B. J. Hoskins. Subtropical anticyclones and summer monsoons. *Journal of Climate*, 14:3192–3211, 8 2001.

[62] Robert Vautard, Kingtse C Mo, and Michael Ghil. Statistical significance test for transition matrices of atmospheric markov chains. *Journal of Atmospheric Sciences*, 47:1926–1931, 1990.

[63] Victor M. Peñaranda-Vélez, Carlos A. Ochoa-Moya, and Arturo Quintanar. ERA5 Daily Mean Sea Level Pressure Anomalies and 100m-Wind Velocity for Mexico and Surrounding Regions, 2026. Available at `https://doi.org/10.7910/DVN/L8AGSP`.

Appendices

A L-Moments

Let X be a continuous random variable with probability distribution $F(x)$ and quantile function $x(F)$. Let $X_{1:n} \leq X_{2:n} \leq \cdots \leq X_{n:n}$ be the order statistics of a random sample of size n, which comes from the same distribution of the random variable X. Given any u, $0 < u < 1$, $x(u)$ as the unique value that satisfies $F(x(u)) = u$, the r-order L-moment of a random variable X is defined as the quantity obtained by evaluating the following expression:

$$\lambda_r = \int_0^1 x(u)\, P^*_{r-1}(u)\, du \tag{18}$$

where,

$$P^*_r(F) = \sum_{k=0}^{r} p^*_{r,k} u^k \tag{19}$$

$$p^*_{r,k} = (-1)^{r-k} \binom{r}{k} \binom{r+k}{k} \tag{20}$$

Thus, the r-order L-moment λ_r is a linear function of the expected value of a certain linear combination of order statistics. Therefore, the first four L-moments of the probability distribution are defined as follows:

$$\lambda_1 = E(X_{1:1}) = \int_0^1 x(F)\, dF \tag{21}$$

$$\lambda_2 = E(X_{2:2} - X_{1:2}) = \int_0^1 x(F)\big[2F(x) - 1\big]\, dF \tag{22}$$

$$\begin{aligned} \lambda_3 =& E(X_{3:3} - 2X_{2:3} - X_{1:3}) \\ =& \int_0^1 x(F)\big[6(F(x))^2 - 6F(x) + 1\big]\, dF \end{aligned} \tag{23}$$

$$\begin{aligned} \lambda_4 =& E(X_{4:4} - 3X_{3:4} + 3X_{2:4} - X_{1:4}) \\ =& \int_0^1 x(F)\big[20(F(x))^3 - 30(F(x))^2 + 12F(x) - 1\big]\, dF \end{aligned} \tag{24}$$

These L-moments can be utilized to characterize the shape of the probability distribution of any random variable X. Similarly, the dimensionless L-moment ratios can be utilized for the estimation of probability distributions, which are defined as: $\tau_r = \lambda_r/\lambda_2$, where $\tau_3 \in (-1, 1)$ is referred to as L-skewness and $\tau_4 \in (-1/4, 1)$ as L-kurtosis. Additionally, the coefficient of L-variation, or L-CV, is defined as: $\tau = \lambda_2/\lambda_1$. Among the properties of L-moments, those pertaining to existence and uniqueness are of paramount importance. The existence property asserts that if the expected value of a distribution is finite, then all its L-moments are finite and a unique distribution exists for the specified L-moments.

B Weibull Distribution

The functional form of the Weibull distribution, used in this research is as follows:

$$F(x) = 1 - \exp\left(- \left[\frac{x - B}{A}\right]^k \right) \tag{25}$$

where A, B, and k are the scale, location and shape parameters, respectively. The quantile function of the Weibull distribution for a given non-exceedance probability F is given by:

$$x(F) = B + A\big[-\ln(1 - F)\big]^{1/k} \tag{26}$$

The L-moments and L-moment ratios that characterize the Weibull distribution are given by:

$$\lambda_1 = B + A\,\Gamma(1 + 1/k) \tag{27}$$

$$\lambda_2 = A(1 - 2^{-1/k})\,\Gamma(1 + 1/k) \tag{28}$$

$$\tau_3 = 3 - \frac{2(1 - 3^{-1/k})}{(1 - 2^{-1/k})} \tag{29}$$

$$\tau_4 = \frac{5(1 - 4^{-1/k}) - 10(1 - 3^{-1/k}) + 6(1 - 2^{-1/k})}{1 - 2^{-1/k}} \tag{30}$$

where $\Gamma(\cdot)$ stands for the Gamma function.

C Kappa Distribution

The four-parameters Kappa Probability Distribution is extensively utilized in regional analysis as a testing distribution for the description of wind velocity fields. The Kappa distribution is defined as follows [40]:

$$F(x) = \left[1 - h\left[1 - \frac{k(x-\xi)}{\alpha}\right]^{1/k}\right]^{1/h} \tag{31}$$

where, ξ is the location parameter, α is the scale parameter, h and k are shape parameters. The quantile function of the Kappa distribution is given by:

$$x(F) = \xi + \frac{\alpha}{k}\left[1 - \left[\frac{1-F^h}{h}\right]^k\right] \tag{32}$$

The upper bound of the Kappa distribution is $\xi + \frac{\alpha}{k}$ if $k > 0$, or ∞ if $k \leq 0$. The lower bound is $\xi + \frac{\alpha(1-h^{-k})}{k}$ if $h > 0$, or $\xi + \frac{\alpha}{k}$ if $h \leq 0$ and $k < 0$, or $-\infty$ if $h \leq 0$ and $h \geq 0$. Among the properties of the Kappa distribution, certain well-known distribution families can be derived from specific parametrizations of the Kappa distribution. When $h = 1$, the Generalized Pareto Distribution (GPD) is obtained; when $h = 0$, the Generalized Extreme Value Distribution (GEV) is obtained; when $h = -1$, the Generalized Logistic Distribution (GLO) is obtained; and when $h = 0$ and $k = 0$, the Gumbel distribution is obtained.